

Contents lists available at ScienceDirect

Renewable Energy

journal homepage: www.elsevier.com/locate/renene





Control-inspired design and power optimization of an active mechanical motion rectifier based power takeoff for wave energy converters

Lisheng Yang ^a, Jianuo Huang ^a, Jia Mi ^a, Muhammad Hajj ^b, Giorgio Bacelli ^c, Lei Zuo ^{a,*}

- a Department of Naval Architecture and Marine Engineering, University of Michigan, Ann Arbor, MI, 48109, USA
- b Department of Civil, Environmental and Ocean Engineering, Stevens Institute of Technology, Hoboken, NJ, 07030, USA
- ^c Sandia National Laboratories, Albuquerque, NM, 87185, USA

ARTICLE INFO

Keywords: Marine energy Wave energy converter Power take-off Motion rectification Control-inspired design Switching system

ABSTRACT

Ocean waves have high energy density and are persistent and predictable. Yet, converting wave energy to a useable form remains challenging. A significant hurdle is the oscillatory nature of waves resulting in the alternating loads, which necessitate the use of rectification at some stage of the energy conversion. This research effort presents a novel design of active mechanical motion rectifier (AMMR) for the power takeoff (PTO), which provides enhanced controllability and better power performance when compared to passive mechanical motion rectifiers (MMR). Inspired by transistors used in synchronous electrical rectifiers, the proposed design uses controllable electromagnetic clutches in the mechanical transmission to allow active engagement-disengagement control; thus, rectifying the oscillatory motion into a unidirectional rotation for high energy conversion efficiency and allowing the generator in unidirectional rotation to control the bidirectional wave capture structure for maximizing the power output. A semi-analytical computational approach is developed to efficiently evaluate the optimal power achieved using the proposed AMMR-based PTO and active control. It is found that the AMMR-based PTO design yields a higher optimal power than the previous passive MMR design across the wave spectrum. The influences of generator inertia and reactive power are discussed. The effects of control parameters on the power output and the optimal trajectories are analyzed. Wave tank tests with the AMMR prototype demonstrated the effectiveness of AMMR based PTO design and validated the numerical analysis.

Nomenclature

$A(\infty)$	Added inertia at infinite frequency	
A_R	Matrix A in the state space realization of radiation impulse function	
A_{ext}	Amplitude of the wave excitation torque	
AMMR	Active mechanical motion rectifier	
$B(\omega)$	Frequency-dependent radiation damping of the flap in pitch	
B_f	Flap's first order viscous damping	
B_R	Matrix B in the state space realization of radiation impulse function	
C_R	Matrix C in the state space realization of radiation impulse function	
d	Engaging duration duty cycle	
h_r	Radiation impulse response convolution kernel	
I	Physical inertia of the floater	
I_{gear1}	Rotational inertia of gear set 1 of AMMR	
I_{gear2}	Rotational inertia of gear set 2 of AMMR	
I_{fw}	Rotational inertia of the generator and attached flywheels	
I_d	Combined flap and drivetrain inertia	
I_g	Generator side rotational inertia, sum of I_{gear2} and I_{fw}	
K	Constant stiffness coefficient of the floater buoyancy	
	(continued on next column)	

⁽continued)

**	m 1 1 0.1 mm 11
K_P	Proportional gain of the PI controller
K_I	Integral gain of the PI controller
MMR	Mechanical motion rectifier
N	Transmission gear ratio from the floater to the generator
PTO	Power take-off
s	Vector of switching times
s_i	Switching time
T	Prediction horizon for the wave excitation torque
T_{ex}	Wave excitation torque
T_{rad}	Wave radiation torque
T_{stat}	Hydrostatic buoyancy torque
T_{pto}	PTO torque acting on the floater
T_{gen}	Generator torque
t_p	Regular wave period
u	Control variable of the generator torque
v_{en}	Engaging velocity of the floater
v_{dis}	Disengaging velocity of the floater
WEC	Wave energy converter

(continued on next page)

E-mail address: leizuo@umich.edu (L. Zuo).

^{*} Corresponding author.

(continued)

X _{en}	System state at clutch engaging time	
X_{dis}	System state at clutch disengaging time	
θ_1	Flap's rotational displacement relative to its equilibrium position	
$\dot{ heta}_2$	Generator's rotational velocity	
θ_{en}	Flap's displacement at clutch engaging time	
θ_{dis}	Flap's displacement at clutch disengaging time	
φ	Engaging phase of the clutch	

1. Introduction

Ocean wave energy has received increasing attention as an alternative renewable energy source over the past two decades. Its large power density puts it as a major player on the road towards a carbon-free future. For instance, ocean wave resources along the US coast alone can provide approximately 34 % of the nation's electricity demand [1]. In addition, ocean waves can complement other renewable energy sources, such as solar and wind, to provide more stable and consistent power supply [2]. Fulfilling the ocean waves' potential requires innovative energy conversion technologies that address unique challenges brought by the oscillatory nature of ocean waves, which necessitates rectification at some stage of the energy conversion. To take advantage of the widespread existing power generation components such as synchronous or induction generators, most wave energy converters (WECs) adopt some kind of motion rectifications to drive the generator in a unidirectional rotation. The simplest form of motion rectification is in overtopping devices where oscillatory waves are guided to surge into a reservoir above the sea surface and then flow down through channels equipped with hydro turbines for energy generation. The Wave Dragon WEC deployed off the coast of Denmark is one example of this type [3]. Although overtopping devices have the advantage of being able to use technologies from the mature hydropower industry, the low water head and flow variations due to irregularity of the waves cause the operation outside the efficient zone of the hydro turbines, driving up the overall cost of wave energy. The oscillating water column (OWC) is another type of WEC that makes use of the up-and-down wave motion to push airflow and drive axis-flow pneumatic turbines [4]. The bidirectional air flow motion can be rectified via either valves [5,6] or specially designed self-rectifying turbines (such as Wells or impulse turbines). Rectifying air flows using valves allows the use of higher efficiency conventional unidirectional turbines but makes it hard to apply reactive control [7]. On the other hand, self-rectifying turbines have much lower efficiency. There have been continuous efforts to improve their efficiency [8–10], but performance enhancements remain limited, especially in reactive control, where the turbine also works as a compressor to give power back to the air flow.

In addition to overtopping devices and OWCs, floater-based WECs have also gained considerable attention. These WECs transfer energy from wave-induced motions of floaters to a generator through motion transmissions. Hydraulic transmissions with check valves and accumulators are employed to build a hydraulic rectifying circuit so that a constant pressure hydraulic motor can be used to drive a unidirectional rotation of the generator [11]. The hydro-fluid rectifying circuit, however, prevents reactive control due to the one-way check valves. Instead, passive phase control methods are adopted for increasing wave power absorption [12,13]. Several studies present alternative designs that aim at enabling reactive control so that the floater's oscillating motion can be controlled more precisely, thus capturing more power from the waves. Ricci et al. introduced separate accumulators storing energy which can be released to drive the floater through controlled valves [14]. In addition, hydraulic manifolds are used to approximate the reactive control discretely [15,16]. Hydrostatic transmission is also used to generate more smooth control [17]. Still, complex structure of hydraulic systems and viscous losses associated with the fluid flow put a limit on the attainable efficiency. The inevitable hydraulic fluid leakage is also a real concern because it can pollute the ocean environment.

In contrast to hydraulic transmissions, mechanical transmissions not only have higher efficiency but also require lower maintenance with lesser environmental impacts [18]. However, the use of pure mechanical transmission is notably absent from large-scale WECs as it is deemed to be incapable of handling large loads. In recent years, there have been studies demonstrating the feasibility of mechanical transmission for WECs, especially by taking advantage of various belt transmissions, which can be scaled up relatively easily [19,20]. Despite the progress, mechanical transmission still faces some obstacles, one of which is the mechanisms for motion rectification [21]. Liang et al. first built and tested a mechanical motion rectification (MMR) PTO for the WEC, using a rack pinion mechanical transmission [22]. Two sets of one-way clutches were used to engage the two pinion gears with one output shaft thus enabling the two oscillatory racks to drive the generator in the unidirectional rotation. This MMR design principle using one-way clutches was later widely extended to other mechanical transmissions to perform motion rectification. Some noteworthy examples include the ball screw transmission designed by Li et al. [23], which can easily integrate a flywheel to the generator, or be modified to couple a current turbine for hybrid wave-current energy conversion [24]. Yang et al. [25] designed a coaxial rectification transmission using four sets of one-way clutches and a planetary gear set. Wu et al. [26] added torsional springs to the transmission to increase its energy storage capability, which can further smooth the generator speed.

These previous studies on MMR design, however, assume only a passive PTO with a constant load. As a result, they treated the PTO damping as a design parameter alongside other PTO parameters like spring stiffness and flywheel inertia. From an optimal control point of view, it is possible to optimally control the instant PTO damping for a given WEC configuration. However, the engagement-disengagement phenomenon makes a WEC with MMR PTO an implicit switching system [27], one of the hardest to solve for optimal control. Moreover, in the abundant WEC control literature [28], the generator torque can be controlled arbitrarily within the physical limits, not necessarily in a damping control form which produces a force negatively proportional to the velocity. In fact, in the WEC control community, it is well known that generally a reactive force is needed to achieve maximum power capture for a WEC [29], meaning the generator needs to sometimes act as a motor to inject reactive power into the WEC system. This capability is not possible when using a passive MMR-based PTO, since all previous designs employ mechanical one-way clutches and thus the MMR based WEC can lose controllability when the system is unclutched for example, when the generator freewheels at high speed (similar as bicycles in downhill motion). Therefore, MMR PTOs are not suitable for reactive

To address the intrinsic limitation in controllability of current MMRbased PTO designs, we propose a new generation of mechanical motion rectifiers, referred to as active MMR (AMMR). The AMMR would allow explicit switching control of the clutches for unidirectional motion rectification and bidirectional power transmission. Thus, it will allow the generator to rotate in one direction at high efficiency and also enable the generator to act as a motor for reactive control. An explicit switching system, whose switching is actively controllable, would be much easier to deal with numerically since many algorithms are available to solve them [30-32]. In addition to introducing a novel AMMR design, this paper presents a semi-analytical power computation approach based on regular wave steady state solution to enable fast evaluation of power capture potential for different WEC configurations using the AMMR PTO. With the proposed approach, the time needed for WEC power evaluation of AMMR PTO is significantly reduced in comparison to time-consuming simulations with a switching nonlinearity. This computational efficiency will enable a control codesign framework to holistically optimize WEC geometric shapes and PTO parameters [33].

This paper is organized as follows. Section 2 introduces the principle of the active mechanical motion rectifier and presents a design of the proposed AMMR. Section 3 presents the WEC modelling used for power

capture analysis. Section 4 details the assumptions and procedures of the proposed power analysis. Then a case study is conducted in Section 5 to analyze the power capture of an oscillating surge WEC with AMMR PTO. Tank tests results are presented for a scaled-down prototype. Section 6 discusses some implications of different generator inertia and proposes several future research directions. The conclusions are presented in section 7.

2. Active mechanical motion rectifier (AMMR) design principle

The design of active mechanical motion rectifiers (AMMR) is in principle an innovation beyond the previously developed passive mechanical motion rectifier (MMR). MMRs are designed for rectifying oscillating bidirectional motion to unidirectional motion. Their working principle is best described through an analogy to electric voltage rectifier, as shown in Fig. 1(a). The voltage and current in the electric rectifier are analogous to velocity and force (or torque in the rotational case) in the MMR [34]. Just as an electrical rectifier uses semiconductor diodes to restrict the electrical current to flow in one direction, a mechanical rectifier uses one-way clutches to restrict the force or torque to transmit in one direction. The three bevel gears act in a similar manner to a center-tapped transformer. Therefore, the bidirectional motion is converted into unidirectional rotation, in a similar way as the AC current is converted into DC current in the electrical rectifier. When operating, the rotational inertia of the output shaft, including the bevel gears, the generator, and optional flywheel, acts as the smoothing capacitor in the electrical rectifier and reduces the fluctuations of the generator rotational speed.

When the input speed is slower, both one-way clutches are disengaged, and the rotational inertia will drive the generator; however, the system loses controllability temporally during this period.

In electrical systems, a controllable rectifier can be implemented by replacing the semiconductor diodes with transistors. Transistors are essentially switches controlled by an external signal. A mechanical counterpart of transistors would allow direct control of the MMR's engagement and potentially control bidirectional power flow while rectifying motion. Inspired by the transistors, the electromagnetic

clutches are identified as an active mechanical transistor to allow active control of the engagement and disengagement, as shown Fig. 2. When the coil in the electromagnetic clutch is energized, the magnetic force will be produced to press the rotor armature against the stator friction pad (Fig. 2(a)). The input and output of the electromagnetic clutch will be engaged. The maximum torque and transient response time will depend on the armature shape, the friction coefficient between the armature and the stator friction lining, and the magnetic field strength [35]. In this paper, clutch dynamics is neglected (since the transient response time is much smaller than the wave period) and we will focus on WEC power capture optimization. Using the electromagnetic clutches, the analogical electric circuit of the AMMR is almost the same as that of MMR except that the diodes are replaced by transistors as shown in Fig. 2. This design allows spur gears or helical gears to be used to change rotation directions. Compared to previous designs that use bevel gears, this configuration also is more reliable since bevel gears are more prone to failure due to installation inaccuracy, larger deformation and higher stress near gear teeth [36].

3. Modelling of a wave energy converter with AMMR power take off

To investigate the power potential of the proposed mechanical PTO type, a simplified model of the AMMR integrated with a generic one degree of freedom (DOF) WEC is derived. The WEC is assumed to have an oscillating body constrained to move in one DOF under wave excitation. Without loss of generality, rotational motion is assumed here and in the following sections. The oscillating body's motion is governed by Newton's second law subject to a combination of different wave induced torques and the PTO torque, written as:

$$I\ddot{\theta} = T_{ex} - T_{rad} - T_{stat} - T_{pto} \tag{1}$$

where I is the physical moment of inertia of the oscillating body itself, θ refers to the body's rotational angle with respect to the equilibrium position. T_{ex} is the excitation torque which comes from the pressure of the wave field's motion. It is the torque exerted on the floater body when

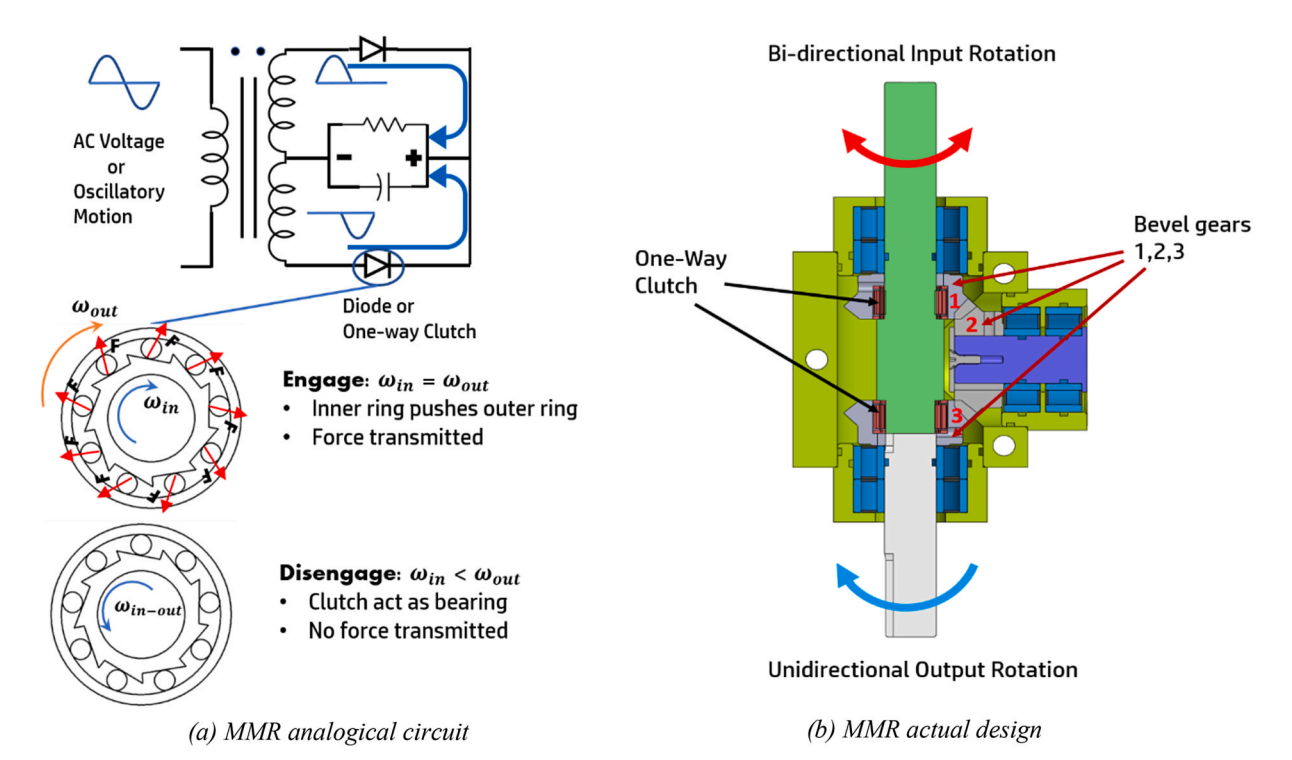
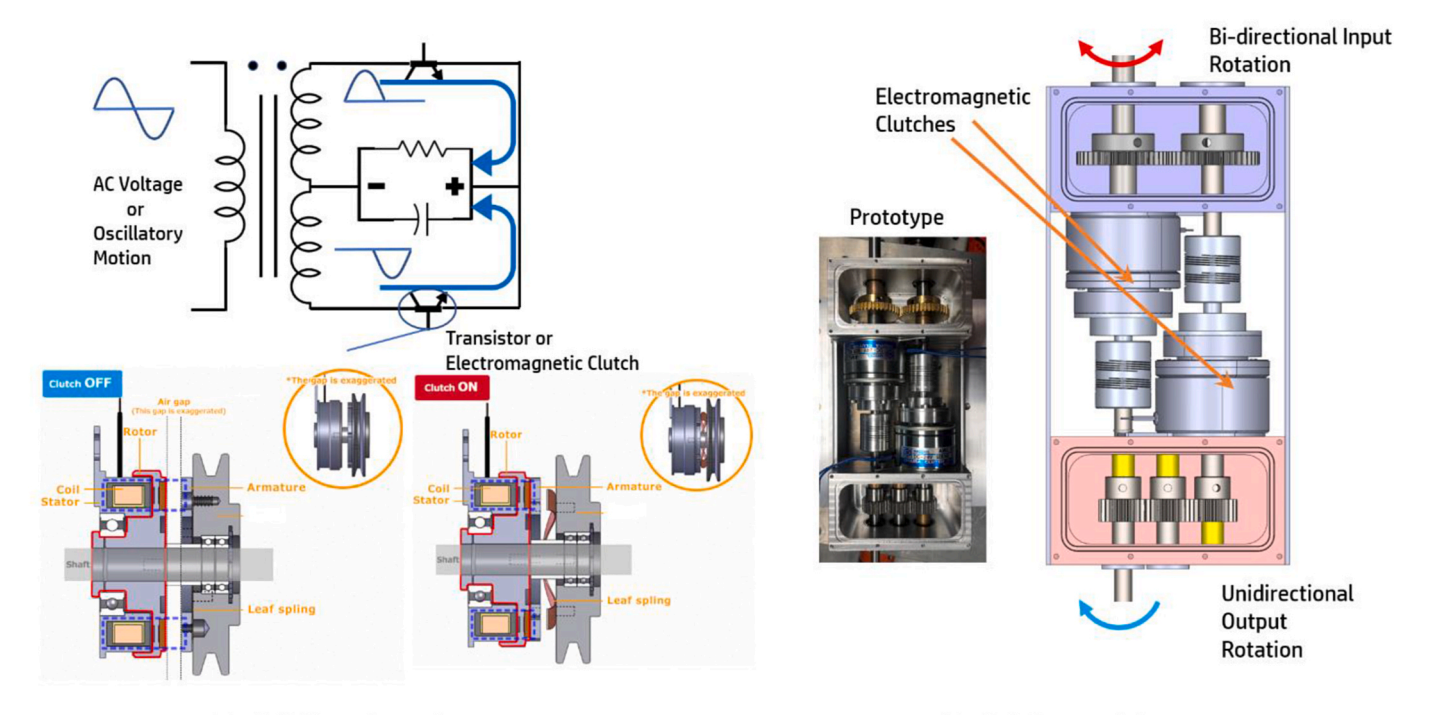


Fig. 1. MMR design principle and analogical electric circuit.



(a) AMMR analogical circuit

(b) AMMR actual design

Fig. 2. AMMR design principle and analogical electric circuit.

it is fixed in place. T_{rad} is the radiation torque which is induced when the floater body oscillates. Physically it comes from the counter pressure when the floater drives its surrounding fluid to generate waves. Both T_{ex} and T_{rad} needs to be computed by integrating wave pressure across the floater's wet surface. By solving or identifying the frequency-dependent coefficients, linear convolution kernels can be constructed to approximate T_{ex} and T_{rad} without the need of integration. Technical details for obtaining the frequency-dependent coefficients numerically and constructing the convolutional kernels can be found in Ref. [29]. T_{stat} is the torque from the static water pressure, which appears as a buoyancy torque and can be approximated as a spring torque with constant stiffness coefficient K when the rotational angle is small: $T_{stat} = K\theta$. T_{nto} is the counter torque from the PTO, which is taken at the connection interface with the floater body as shown in Fig. 3. The AMMR PTO is simplified as two parts separated by the controllable clutches. The first part is the set of gears attached to the input shaft, which rotate

bidirectionally with the oscillating body. The second part is the set of gears attached to the output shaft, which rotate unidirectionally with the generator. When one of the clutches is engaged, both Gears1 and Gears2 rotate together with the oscillating body, their motion is governed by:

$$(I + N^2(I_{gear1} + I_{gear2} + I_{fw}))\ddot{\theta} + K\theta = T_{ex} - T_{rad} - NT_{gen}$$
(2)

Here I_{gear1} is the rotational inertia of Gears1, I_{gear2} is the rotational inertias of Gears2, and I_{fw} is the combined inertia of the generator and attached flywheels. N is the transmission ratio from the oscillating body motion to the input shaft of the AMMR PTO. T_{gen} is the torque applied by the generator. When both controllable clutches are disengaged, the governing equation is given by:

$$(I + N^2 I_{gear1}) \ddot{\theta} + K \theta = T_{ex} - T_{rad}$$

$$(I_{gear2} + I_{fw}) \ddot{\theta}_{gen} = T_{gen}$$

$$(3)$$

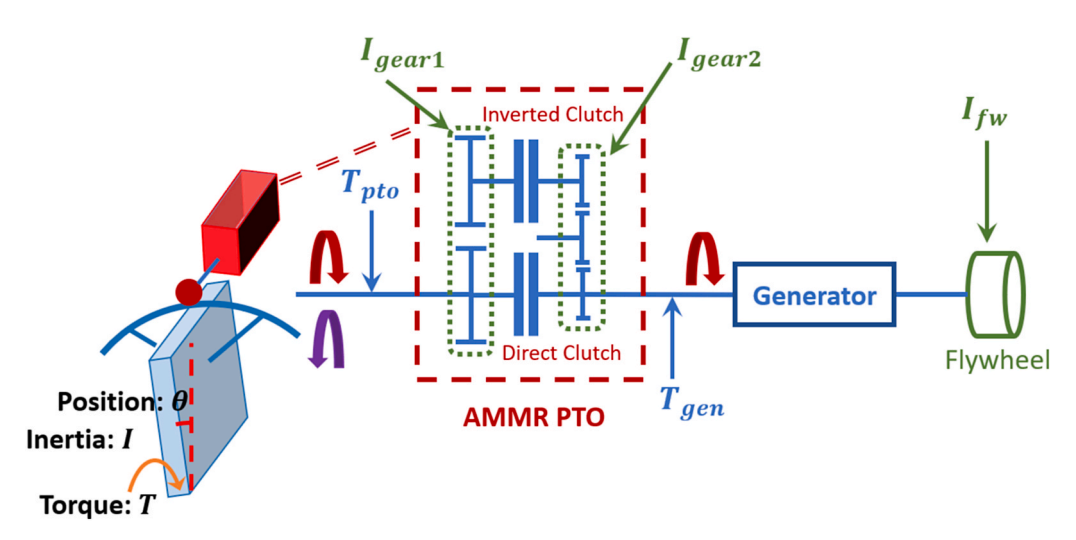


Fig. 3. Simplified modelling of the AMMR PTO.

During disengagement, the generator side inertia I_{gear2} continues to rotate in one direction, and the electromagnetic torque applied by the generator solely determines its motion (note that generator mechanical damping or friction is neglected here). This means the generator side inertia's motion is fully controllable during disengagement. It is noted that, on the other hand, the oscillating body's motion during disengagement is uncontrollable. However, unlike the passive MMR, we can actively control the engagement whenever needed.

4. A semi-analytical approach for wave energy converter optimal power evaluation with AMMR power take off

For a mechanical PTO that is always connected to the oscillating body, the WEC's dynamics is linear and its theoretical optimal power can be obtained using the principle of impedance matching for each excitation frequency. For the AMMR PTO, however, the WEC's dynamics is no longer linear with system switching entailed due to its motion rectification to enable unidirectional rotation of the generator. Therefore, a new approach is needed to determine its theoretically achievable maximum power. As ocean wave power is usually concentrated over a frequency band, it is plausible to first evaluate the optimal power under regular waves at each individual frequency.

4.1. AMMR optimal power formulation and assumptions under regular waves

Compared to a conventional direct-connected mechanical PTO, the biggest difference of the AMMR PTO is that it needs active control of the clutch engagement for rectification. This presents unique challenges as the control of clutches introduces discrete decision variables into the conventional optimal control problem, which typically only involves control of the continuous generator torque. To explain further, the engaging and disengaging dynamics of the AMMR WEC are first defined. The positive engagement dynamics is governed by:

$$\begin{aligned}
\left(I + N^2 \left(I_{gear1} + I_{gear2} + I_{fw}\right)\right) \ddot{\theta}_1 &= T_{ex} - Nu - K\theta_1 - T_{rad} \\
\dot{\theta}_2 &= N\dot{\theta}_1
\end{aligned} \tag{4}$$

where $\dot{\theta}_1$ is the oscillating body's velocity while $\dot{\theta}_2$ is the generator's velocity. Similarly, the negative engagement dynamics is governed by:

$$\left(I + N^2 \left(I_{gear1} + I_{gear2} + I_{fw}\right)\right) \dot{\theta}_1 = T_{ex} + Nu - K\theta_1 - T_{rad}
\dot{\theta}_2 = -N\dot{\theta}_1$$
(5)

The disengagement dynamics are governed by two equations for two sides of the controllable clutches:

$$(I + N^{2}I_{gear1})\ddot{\theta}_{1} = T_{ex} - K\theta_{1} - T_{rad}$$

$$(I_{gear2} + I_{fw})\ddot{\theta}_{2} = u$$
(6)

Although there are three operation states of the AMMR PTO, mathematically only two sets of equations are needed to represent the switching dynamics. This is because the positive and negative engaging states only differ in the signs of $\dot{\theta}_2$ and u. Since $\dot{\theta}_2$ is not influencing the dynamics and u is the control variable, this sign change can be ignored so that one set of equations is used to represent the engaging dynamics. The radiation torque can be represented by the Cummins equation [37]: $T_{rad}(t) = -A(\infty) \ddot{\theta}_1 - \int_0^t h_r(t-\tau) \dot{\theta}_1(\tau) d\tau$, where the convolution kernel h_r can be considered as the impulse response of a linear system described in state space form as:

$$\dot{X}_R = A_R X_R + B_R \dot{\theta}_1$$

$$\int_0^t h_r(t - \tau) \dot{\theta}_1(\tau) d\tau = C_R X_R$$
(7)

These representations lead to a simplified form of the governing equations of the engaging dynamics, which are written as:

$$\mathbf{f}_{1}: \frac{\ddot{\theta}_{1} = \left(T_{ex} - Nu - K\theta_{1} - C_{R}X_{R}\right) / \left(I + A(\infty) + N^{2}\left(I_{gear1} + I_{gear2} + I_{fw}\right)\right)}{\dot{X}_{R} = A_{R}X_{R} + B_{R}\dot{\theta}_{1}} \\ \dot{\theta}_{2} = N\dot{\theta}_{1}$$
(8)

Here X_R is the realized state of the state space system for the radiation kernel. The disengaging dynamics can be similarly represented by:

$$\dot{\theta}_{1} = \left(T_{ex} - K\theta_{1} - C_{R}X_{R}\right) / \left(I + A(\infty) + N^{2}I_{gear1}\right)
\mathbf{f}_{2}: \dot{X}_{R} = A_{R}X_{R} + B_{R}\dot{\theta}_{1}
\left(I_{gear2} + I_{fw}\right)\ddot{\theta}_{2} = u$$
(9)

Letting **[0, T]** be the prediction horizon where the excitation torque $T_{ex}(t)$ is predicted and defining the set of the clutch switching time vector as $\triangleq \{\mathbf{s} \in \mathbb{R}^n : s_{i-1} \leq s_i, i=1,...,n+1\}$, where $s_0=0$ and $s_{n+1}=\mathbf{T}$, the optimal control problem is formulated as:

$$\underline{\min_{\mathbf{s} \in S, u(t) \in [u_{lb}, u_{ub}]}} = \sum_{i=0}^{n} \int_{s_i}^{s_{i+1}} \dot{\theta}_2(t) u(t) dt \tag{10}$$

s.t.
$$\dot{\mathbf{x}} = \mathbf{f}_k(\mathbf{x}, u), t \in [s_i, s_{i+1}), k = 1, 2$$

Depending on the initial state, the sequence of the switching dynamics can be fixed, alternating between engaged state and disengaged state. Still, solving problem (10) is computationally challenging especially as it is difficult to get the gradients of switching time vector s. For a control co-design process, it is important to have a fast evaluation method of the WEC's optimal power under control, so that the WEC's design parameters are optimized under a rapid iterative optimization framework. In order to simplify problem (10), three assumptions are made.

- (i) Regular waves at individual frequencies are considered, i.e., ${\bf T}=t_p,T_{ex}(t)=A_{ex}\sin\omega t,\omega=2\pi/t_p$
- (ii) s ∈ R⁴, which implies that there are at most four clutch switches in a regular cycle.
- (iii) The state values are continuous across clutch switches.

Assumption (ii) is based on the observation that there are two zero crossings of T_{ex} in a cycle, and at least two switches are needed to achieve rectification for one zero crossing. Although more switches are possible, increasing the dimension of s increases the complexity of problem (10). Also, from a practical standpoint, switching clutches comes with losses so it is better to avoid unnecessary switching. Assumption (iii) is needed to address the jumps in the state value during the transition from dynamics f_2 to f_1 . During this reengaging process, the clutch friction pad synchronizes the main body velocity $\dot{\theta}_1$ and the generator velocity $\dot{\theta}_2$ in a perfectly inelastic collision, leading both values to jump from s_i^- to s_i^+ (s_i^\pm is the left/right limit to s_i). Note from (8) that during the disengaged state f_2 , the generator's dynamics is fully decoupled from the oscillating body's dynamics and its motion is fully controllable and the time constant is much smaller than the wave period. As such, $\dot{\theta}_2$ can be controlled to synchronize with $\dot{\theta}_1$ before reengaging, eliminating state value jumps. This assumption is made to avoid complexities associated with the state jump and should have no negative impact on the generated power. Although the instantaneous power during the disengagement depends on the decoupled generator velocity $\dot{\theta}_2$ and generator torque u, the average power only depends on the oscillating body's velocity $\dot{\theta}_1$. This is because the power source of the system comes from the wave excitation, and the power absorbed equals the input power from the wave $T_{ex}\dot{\theta}_1$ minus the radiated power from the body $T_{rad}\dot{\theta}_1$.

4.2. A semi-analytical approach for AMMR optimal power computation

With the above assumptions, a semi-analytical approach is developed for fast evaluation of the optimal control problem (10). This approach further assumes the switching time vector \mathbf{s} is symmetric during a regular wave cycle, since the sinusoidal excitation force input is symmetric. Essentially, the repeating cycle is half of the wave period after rectification, so the components of \mathbf{s} satisfy $0 \le s_1 \le s_2 \le t_p/2 \le s_3 \le s_4 \le t_p$ with $s_3 = s_1 + t_p/2$ and $s_4 = s_2 + t_p/2$. This assumption reduces the timing vector to be determined by only two parameters.

Let φ be the phase of engaging time relative to the excitation force and d be the engaging duration duty cycle as a percentage of the whole wave cycle. Then, if at time 0 the system is disengaged, $s_1 = t_p \varphi/(2\pi)$ and $s_2 = s_1 + t_p d/2$, as shown in Fig. 4 (a). If at time 0 the system is engaged, $s_2 = t_p \varphi/(2\pi)$ and $s_1 = s_2 - t_p (1-d)/2$, as shown in Fig. 4 (b). It is evident that the parameter space of $\varphi \in [0,\pi)$ and $d \in (0,1]$ spans the symmetric vector space s and can be a more compact substitute for clutch switching time representation. Similar to the time vector, the control trajectory is also assumed to be symmetric. Then the system has periodic responses under regular wave excitations at steady state. This periodic steady state response is observed during simulations as shown in Fig. 5 with X_{en} representing the system state at the moment of engagement including position θ_{en} and velocity v_{en} , while X_{dis} representing the system state at the moment of disengagement including position θ_{dis} and velocity v_{dis} .

In addition, the system's states are also symmetric between the positive and negative half cycles. Assuming such periodic and symmetric responses exist for a symmetric clutch switching time schedule and control trajectory, the instantaneous power generation is also periodic. Then, the objective function of the optimal control problem (10) can be substituted by the average power for regular wave cases as shown below:

from the disengaging dynamics $\mathbf{f_2}$ in Equation (6). Due to assumption (iii) in the previous section, the generator velocity $\dot{\theta}_2$ is always synchronized with the body velocity $\dot{\theta}_1$ before the engaging moment. Therefore, it is enough to only know the oscillating body's velocity $|\nu_{en}|$ and $|\nu_{dis}|$ at the switching moments. Lastly, it is shown below that ν_{en} and ν_{dis} can be solved through a set of equations by leveraging the periodicity and an analytical solution of linear systems.

For a linear WEC system, it is found that a PI controller with velocity/position feedback is sufficient to achieve the power upper bound for a harmonic excitation [38]. Because the AMMR leads to a nonlinear switching system, the PI control may not achieve the upper bound. Still, it provides a convenient starting point with only two gains to be optimized. Such a feedback controller can be used during the engaging stage so that $u(t) = K_I \theta_1 + K_P \dot{\theta}_1$. Then, the engaging and disengaging dynamics of Equations (7) and (8) are written in a state space form as:

$$\begin{bmatrix} \dot{\theta}_1 \\ \ddot{\theta}_1 \\ \dot{X}_R \end{bmatrix} = \begin{bmatrix} \mathbf{0} & \mathbf{1} & \mathbf{0} \\ -K + NK_I & NK_P & -C_R \\ I_{en} & I_{en} & I_{en} \\ \mathbf{0} & B_R & A_R \end{bmatrix} \begin{bmatrix} \theta_1 \\ \dot{\theta}_1 \\ X_R \end{bmatrix} + \begin{bmatrix} \mathbf{0} \\ \frac{1}{I_{en}} \\ \mathbf{0} \end{bmatrix} T_{ex} \sin(\omega t)$$
(12)

with
$$I_{en} = I + A(\infty) + N^2 \left(I_{gear1} + I_{gear2} + I_{fw}\right)$$

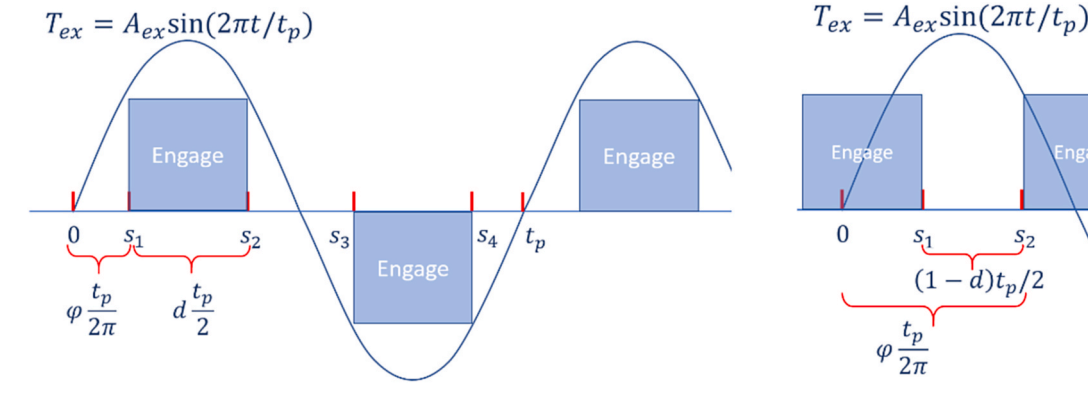
$$\begin{bmatrix} \dot{\theta}_{1} \\ \ddot{\theta}_{1} \\ \dot{X}_{R} \end{bmatrix} = \begin{bmatrix} 0 & 1 & \mathbf{0} \\ \frac{-K}{I_{dis}} & 0 & \frac{-C_{R}}{I_{dis}} \\ \mathbf{0} & B_{R} & A_{R} \end{bmatrix} \begin{bmatrix} \theta_{1} \\ \dot{\theta}_{1} \\ X_{R} \end{bmatrix} + \begin{bmatrix} \mathbf{0} \\ \frac{1}{I_{dis}} \\ \mathbf{0} \end{bmatrix} T_{ex} \sin(\omega t)$$
with $I_{dis} = I + A(\infty) + N^{2}I_{eear1}$ (13)

For constant control gains K_I and K_D , these turn out to be linear time

$$\min J(\varphi, d, u) = 2 \left(\int_{\varphi t_p/(2\pi)}^{\varphi t_p/(2\pi) + t_p d/2} \dot{\theta}_1(t) u(t) dt + \frac{1}{2} N^2 \left(I_{gear2} + I_{fw} \right) \left(v_{dis}^2 - v_{en}^2 \right) \right) / t_p$$
(11)

First, due to symmetric control and response, the repeating cycle of the instantaneous generated power is half of the wave period. So, only half cycle energy needs to be calculated. Second, it is noted that the harvested energy during the disengage stage can simply be represented by the kinetic energy difference of the rotational inertia at the generator side between disengaging moment and engaging moment, as can be seen

invariant (LTI) systems with harmonic inputs. The state response of LTI system $\dot{X}=AX+Bu$ is $X(t)=e^{A(t-t_0)}X(t_0)+\int_{t_0}^t e^{A(t-\tau)}Bu(\tau)d\tau$. When the system input is harmonic such as Equations (12) and (13), the convolutional integral term has an explicit expression. To show this, the engaging dynamics (12) is rewritten in matrix form as:



(a) At time 0 the system is disengaged

(b) At time 0 the system is engaged

Fig. 4. Symmetric timing vector s determined by engaging phase and duty cycle.

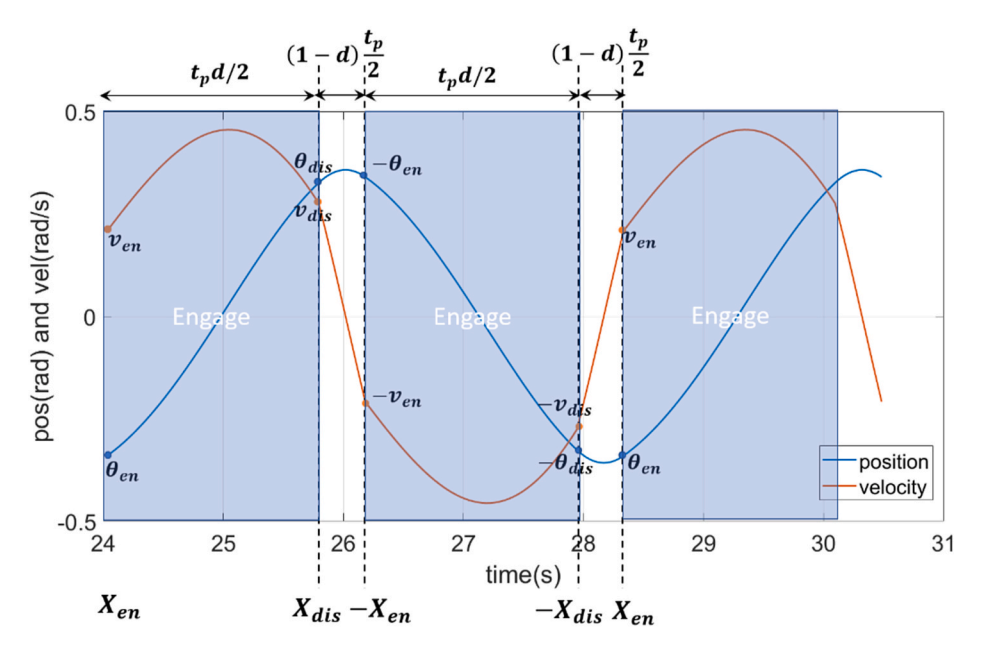


Fig. 5. Periodic and symmetric response of the oscillating WEC body motion $heta_1$

$$\dot{X} = A_1 X + T_{ex} B_1 \Im \left(e^{i\omega t} \right) \tag{14}$$

Then, the system state response is:

$$X(t) = e^{A_1(t-t_0)}X(t_0) + T_{ex}\Im\left(\int_{t_0}^t e^{A_1(t-\tau)}e^{i\omega\tau}d\tau\right)B_1$$
(15)

Through integration by parts, the convolutional integral is solved explicitly, leading to the final response expression:

$$X(t) = e^{A_1(t-t_0)}X(t_0) + T_{ex}\Im\Big((i\omega I - A_1)^{-1} \Big(Ie^{i\omega(t-t_0)} - e^{A_1(t-t_0)}\Big)B_1e^{i\omega t_0}\Big)$$
(16)

Similarly, the disengaging dynamics (13) is rewritten in matrix form

$$\dot{X} = A_2 X + T_{ex} B_2 \Im \left(e^{i\omega t} \right) \tag{17}$$

and exhibits similar responses. Based on the state periodicity and symmetry relationship shown in Fig. 5, for one cycle the state moves from X_{en} (positive engaging) to X_{dis} (positive disengaging) to $-X_{en}$ (negative engaging) to $-X_{dis}$ (negative disengaging) and back to X_{en} . Then, the equations

$$X_{dis} = e^{A_1 t_p d/2} X_{en} + T_{ex} \Im \left((i\omega I - A_1)^{-1} \left(I e^{i\omega (t_p d)/2} - e^{A_1 (t_p d)/2} \right) B_1 e^{i\varphi} \right)$$
(18)

$$-X_{en} = e^{A_2(1-d)t_p/2}X_{dis} + T_{ex}\Im((i\omega I - A_2)^{-1}(Ie^{i\omega(1-d)t_p/2} - e^{A_2(1-d)t_p/2})B_2e^{i(\varphi+d\pi)})$$
(19)

can be set to solve for X_{en} and X_{dis} . Once X_{en} and X_{dis} are determined, the average power in Equation (11) can be evaluated. The power expression in Equation (11) after substituting in the feedback control is then written as:

$$\begin{aligned} \textit{Power} &= 2 \bigg(\int_0^{t_p d/2} \big(K_I \theta_1 \dot{\theta}_1(t) + K_P \dot{\theta}_1^2(t) \big) dt + \frac{1}{2} N^2 \big(I_{gear2} + I_{fw} \big) \Big(v_{dis}^2 \\ &- v_{en}^2 \big) \bigg) \bigg/ t_p \end{aligned} \tag{20}$$

Here v_{en} and v_{dis} are the second state components of X_{en} and X_{dis} . With X_{en} known, the state response function during the engaging stage is known as:

$$X(t) = e^{A_1 t} X_{en} + T_{ex} \Im \left((i\omega I - A_1)^{-1} \left(I e^{i\omega t} - e^{A_1 t} \right) B_1 e^{i\varphi} \right)$$
(21)

Then $\theta_1(t)$ and $\dot{\theta}_1(t)$ are known as the first and second state components of X(t), and expression 20 can be rapidly evaluated.

Finally, it's worth pointing out that although the AMMR makes the WEC system nonlinear, it still preserves some linear system properties. One important property is that changing the excitation amplitude does not change the optimal control parameters. This can be seen from Equation (18)–(21). When T_{ex} changes, X_{en} and X_{dis} change in proportion, leading to the resulting state trajectory also changing in proportion. Then, the power changes proportional to the square of the excitation change.

5. Oscillating surge wave energy converter case study

In this section, an oscillating surge wave energy converter (OSWEC) is selected to demonstrate the proposed method for evaluating the WEC's power performance using the AMMR PTO. The OSWEC is a single degree of freedom flap that pierces the free surface. It is positioned perpendicular to the wave directions and undergoes an oscillatory rotational motion as the wave's crest and trough pass by its free end [39]. It has been shown to have broadband power absorption characteristics [40], which make it suitable to evaluate power across a wide wave spectrum. In Subsection 5.1, the chosen surge flap's dimensions are presented, along with its hydrodynamics properties. Numerical analysis results under regular waves are presented in Subsection 5.2 to investigate how different design and control variables influence the WEC's power. Finally, in Subsection 5.3 tank test results of the flap WEC with AMMR PTO are presented to validate the numerical analysis and demonstrate the effectiveness of the proposed design.

5.1. Properties of an oscillating surge flap moving in the pitch mode

The shape and mass properties of the flap, schematically presented in Fig. 6, were tuned to have maximum response amplitude when excited by 9-s waves in the full scale, which corresponds to a common median wave period in the Pacific Ocean. The waves of interest have periods ranging from 5 to 15 s, which cover most sea conditions. The added mass, radiation damping, and excitation torque properties of the flap body are frequency dependent. Fig. 7(a–c) shows their values over the

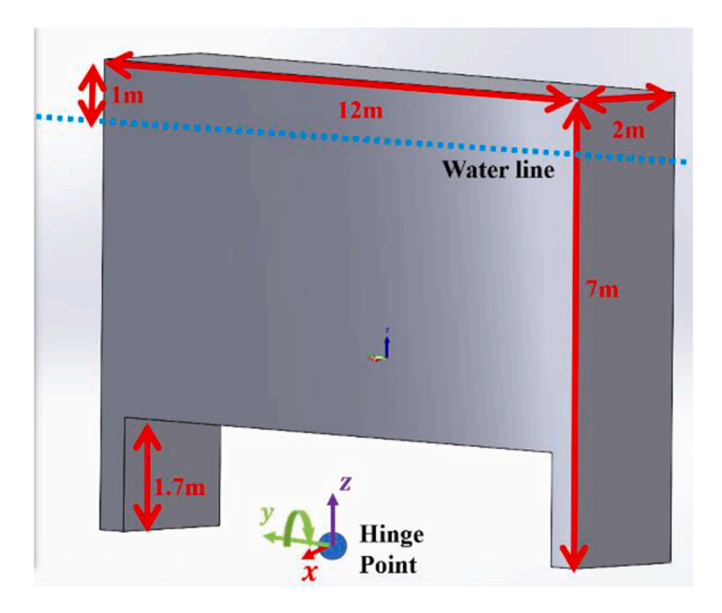
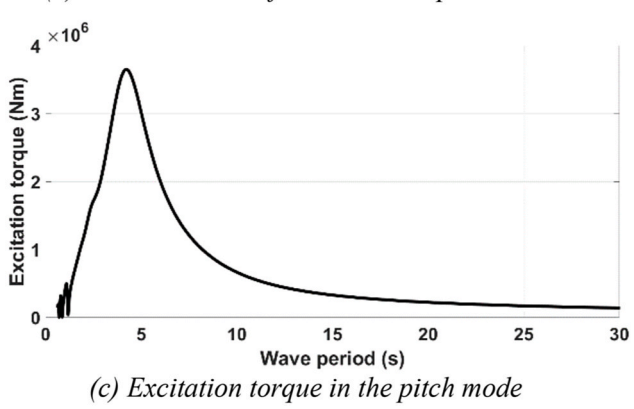


Fig. 6. Geometry dimensions of the oscillating flap.

wave spectrum range calculated by the boundary element method (BEM) solver Nemoh. It is noted that the excitation torque applied by the waves rapidly increases when the wave periods are shorter than 10 s. This leads to larger power potential over the short wave periods for this specific flap, although incident wave power generally increases with wave periods. The radiation damping also exhibits sharp increases when wave periods get shorter than 10 s. For waves with periods longer than 9 s, the radiation damping is very small. The added inertia is also larger over the shorter wave periods, which makes the system's resonance period longer than the wave periods in this range, creating a mismatch in terms of resonance. When considering the whole WEC system,

(a) Added moment of inertia in the pitch mode



significant PTO mechanical damping needs to be added on top of the radiation damping, and the rotational gear inertia also adds to the flap's moment of inertia. For the purpose of this investigation, reasonable estimates of these constant drivetrain inertia and damping are used to reflect the real operation. Those values are summarized in Table 1.

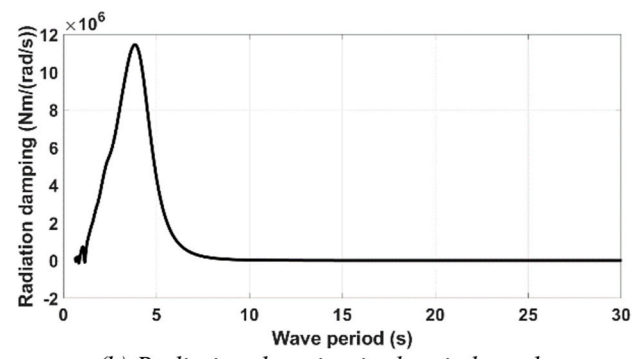
For the WEC system, one of the most important properties is its impedance, which determines its oscillation response under forced excitations and defined as:

$$\frac{T(\omega)}{Z(\omega)} = \Omega(\omega)$$
 (22)
$$Z(\omega) = B(\omega) + B_f + i(\omega(I + A(\omega)) - K/\omega)$$

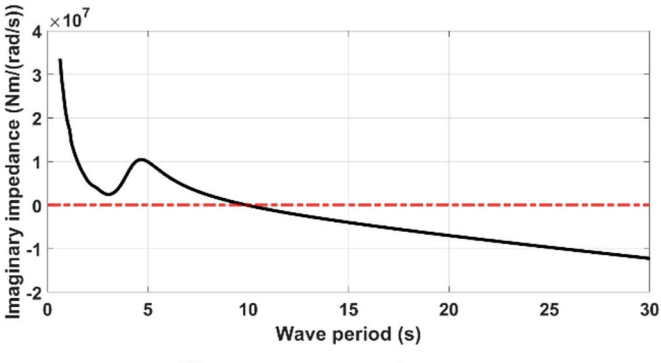
where $T(\omega)$ is the total external torque applied on the flap including wave excitation and PTO counter torque, while $\Omega(\omega)$ is the resulting rotational velocity. The real part of the impedance is the sum of the flap's radiation damping $B(\omega)$ and viscous damping B_f , while the

Table 1 Evaluated parameter values.

Symbol	Values	Meaning
B_f	$5\times10^5~\text{Nm/(rad/s)}$	Drivetrain mechanical
		damping
I_d	$8.53 \times 10^5 \mathrm{Kgm}^2$	Flap and drivetrain inertia
K	2.85×10^6 Nm/rad	Flap buoyance stiffness
I_g	0.5×10^6 , 2×10^6 ,, 6.5×10^6 Kgm ²	Generator side gear/flywheel
		inertia
φ	$0, 0.1\pi,, 0.9\pi$	Engaging phase
d	20 %, 25 %,, 90 %	Engaging duty cycle
K_I	-2.85×10^6 , -1.425×10^6 ,, $2.85 \times$	PI control integral gain
	10 ⁶ Nm/rad	
K_{D}	$-1.25 \times 10^5, -2.5 \times 10^5,, -2.5 \times$	PI control proportional gain
P	10 ⁷ Nm/(rad/s)	1 1 1 1 1 0
t_p	5, 6,, 15 s	Wave period



(b) Radiation damping in the pitch mode



(d) Imaginary impedance

Fig. 7. Hydrodynamic properties of the oscillating flap.

imaginary part of the impedance is related to the flap's physical and added inertia as well as the buoyancy stiffness. When the imaginary value is zero, the WEC's velocity is in phase with the excitation force, yielding the natural resonance period. Fig. 7 (d) shows the plot of imaginary impedance value. It can be seen the system's natural period is around 10 s.

5.2. Wave energy converter power investigation with AMMR

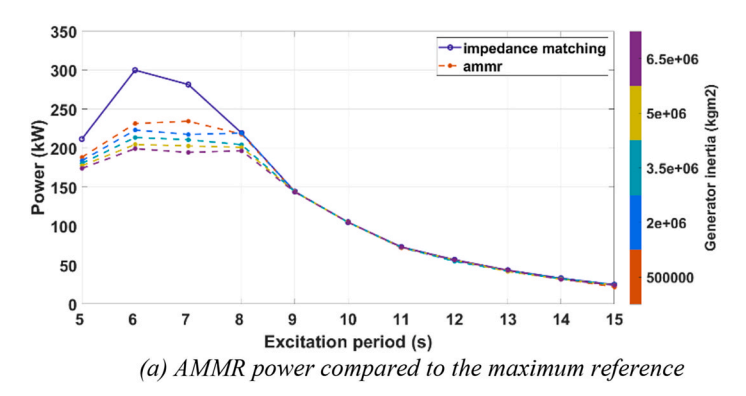
When adopting the AMMR-based PTO, the regular wave optimal power no longer has a clean closed-form solution due to discontinuities introduced by the rectification process. Using the semi-analytical approach developed in Section 4, this subsection details the influences of different design and control parameters on the WEC power capture. An approximate optimal power can be obtained by examining a combination of possible discrete parameter values spanning across their feasible ranges. The sweeping of parameter values also allows detailed analysis of parameter variation. Table 1 summarizes the parameter values swept in this study. All of the drivetrain inertia and damping are equivalent values after considering the gear ratio. The generator side inertia I_g includes both the gearsets I_{gear2} and an optional flywheel, which can have different inertia to adjust I_g . The flap side inertia I_d includes inertia of the flap I and the equivalent inertia of drivetrain gearsets I_{gear1} that are always connected to the flap. In this study, I_d is deemed fixed and I_g is the design variable. Five levels of I_g are considered, ranging from one sixth to more than twice the oscillating part inertia (which includes I_d and the water added inertia). The control variables include clutch control variables φ , d, and generator control variables K_I and K_p . The engaging phase, φ , is discretized into ten even values across one half cycle of the excitation torque. The engaging duration, d, is discretized into fifteen levels ranging from 20 % to 90 %. 100 % engaging is not considered here as the system becomes linear and its power can be easily evaluated using linear theory. The velocity feedback proportional gain K_p takes only negative values, aimed at providing a generator damping torque that acts as the main way for power absorption. Two hundred even discrete values are evaluated with the maximum set by the shorted damping coefficient of a 300 kW generator. The position feedback integral gain K_I determines the generator's reactive forces which can adjust the overall system's stiffness. For a non-switching always engaging linear system, the work of reactive forces always integrates to zero and thus does not contribute to the absorbed power. It is not necessarily the same case for the switching rectification system. Still, five values of K_I are considered to evaluate how adjusting the system's stiffness can influence the AMMR WEC system. The corresponding five levels of system stiffness range from no stiffness to double the original buoyance stiffness. Wave heights of 1 m are considered for all regular waves studied here.

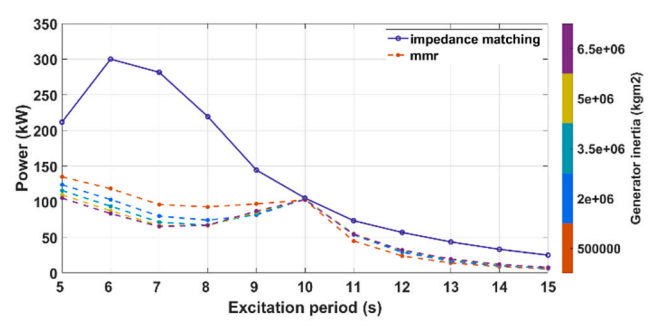
 Comparison between AMMR and MMR PTOs against the impedance matching optimal conditions

By evaluating all the parameter value combinations listed in Table 1, the largest achieved power is plotted for five different generator inertia levels in Fig. 8 (a). For an MMR PTO, simulations were run to evaluate the largest power across the two hundred generator damping coefficients K_p , and the results are shown in Fig. 8 (b) for the five generator inertia levels. The theoretical maximum with the well-known impedance matching condition [38] is also calculated and plotted as a reference. Note that with impedance matching, the inertia levels don't influence the maximum power. This is because inertia only affects the imaginary part of the WEC impedance, which is canceled by the impedance matching.

Fig. 8 shows that the AMMR PTO has significant improvements over the MMR PTO in terms of power performance. In fact, for wave periods longer than 8 s, AMMR PTO can almost achieve the same level of power as the theoretical maximum under impedance matching, which indicates its great power potential. In contrast, the MMR PTO can only achieve the theoretical maximum at the 10 s resonance period. This suggests that while the MMR PTO might be sufficient if the WEC operates at resonance, the AMMR can adapt to more broadly varying wave conditions where the WEC operates off resonance. Moreover, the generator inertia, which has a considerable effect on power performance with MMR PTO, does not affect the AMMR's power as much. As shown in Fig. 8 (b), for the MMR PTO, smaller generator inertia tends to have more power when the wave period is shorter than the resonance period, and larger generator inertia tends to have more power when the wave period is longer than the resonance period. The reason for this inertia difference can be intuitively seen from the steady state time domain response shown in Fig. 9 (the wave excitation unit is normalized in Figs. 9 and 10 for visualization). At short waves, small inertia generator can achieve higher velocity amplitude as shown in Fig. 9 (a); while at longer waves, large inertia has better phase alignment with the excitation torque and higher average speed due to disengaged freewheeling. On the other hand, with AMMR's active clutch control, different generator inertia wouldn't influence the engagement time. And the optimally controlled engagement time schedule can enforce a good phase alignment between the flap velocity and excitation torque as shown in Fig. 10. It is important to note that in this paper the AMMR's steady state response is computed analytically, therefore the time axis in the plot is only for illustration purpose and does not mean real simulation time. By adjusting the engagement control gains, the flap's velocity amplitude of different inertia can also be controlled to be around the same optimal value. This leads to similar levels of power absorption among different generator inertia levels. Therefore, the generator inertia's selection can be decided solely by PTO efficiency rather than considering its influences on power capture potential.

Fig. 11 (a) plots the WEC's displacement amplitude with the AMMR PTO when it is controlled to produce the largest power. Fig. 11 (b) plots





(b) MMR power compared to the maximum reference

Fig. 8. Largest power obtained by AMMR and MMR PTO with different generator inertia.

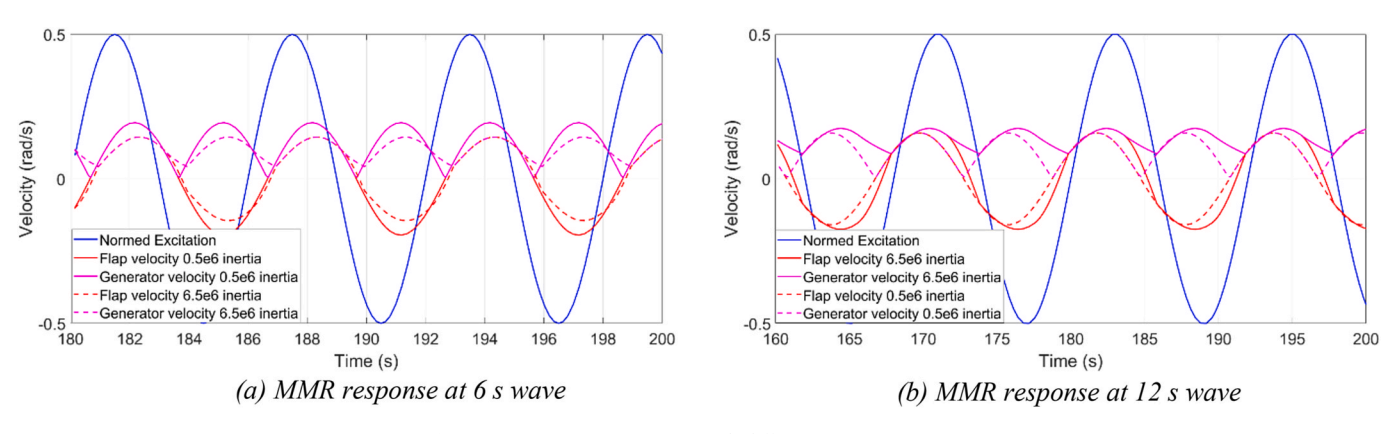


Fig. 9. Passive MMR responses with different generator inertia.

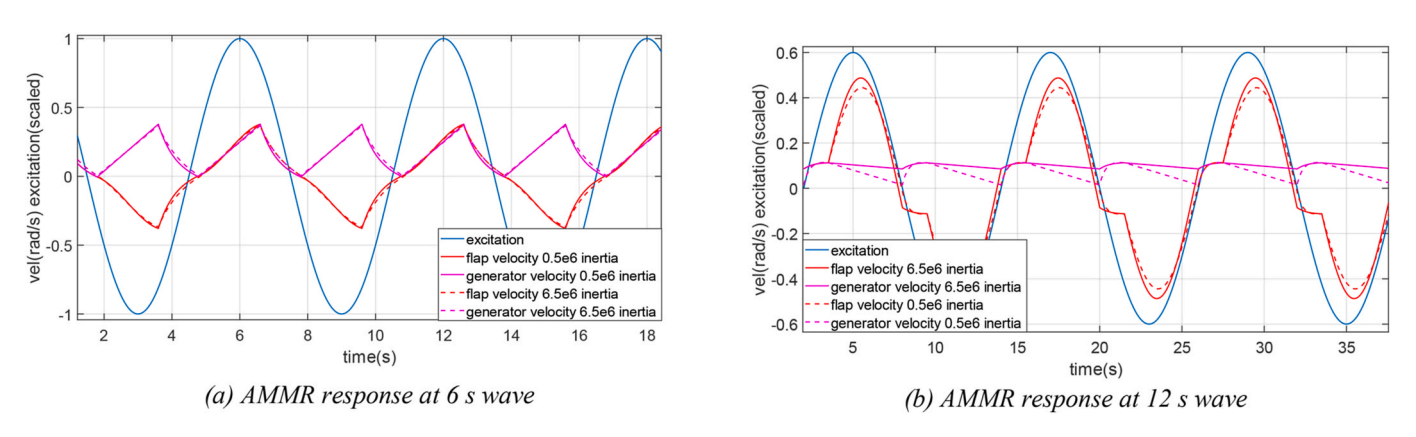


Fig. 10. Active MMR responses with different generator inertia.

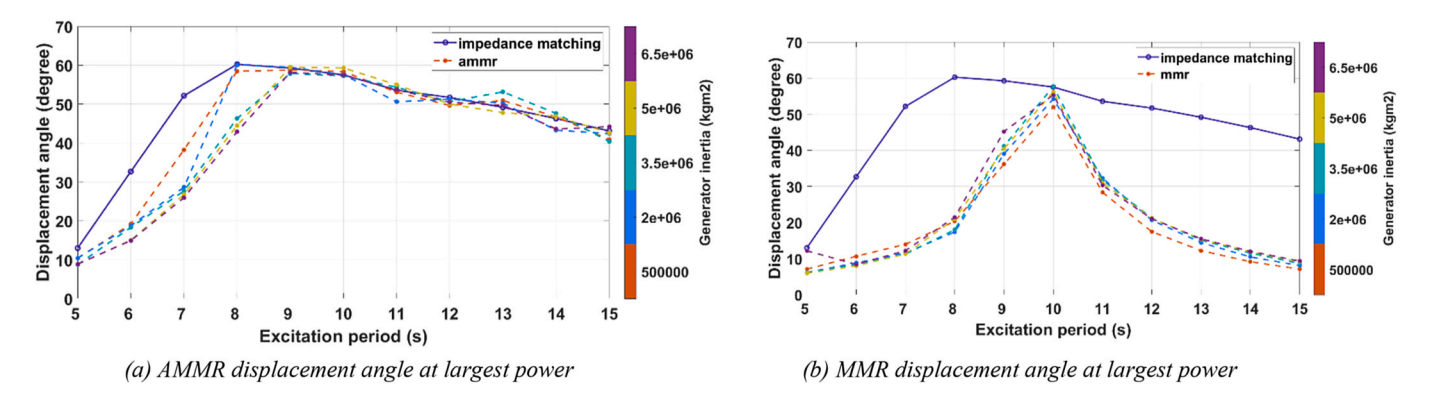


Fig. 11. WEC Displacement amplitude at the largest power for AMMR and MMR.

the displacement amplitude with the MMR PTO at the largest power. In both figures, the WEC displacement amplitude under impedance matching is plotted as a reference. Compared with Fig. 8, it is noted that larger power corresponds to larger movement amplitude, regardless of which PTO or control is applied. Also, for most wave periods, the AMMR WEC would need to go above 30° to achieve the optimum, violating the linear buoyance stiffness assumption. In this sense the power shown in Fig. 8 is only an upper bound indicating the AMMR's power potential under linear wave theory. Still, relatively speaking, the AMMR PTO certainly outperforms the MMR PTO in terms of power performance. It increases power by as much as two folds at short waves and as much as three folds at long waves compared to MMR PTO.

(2) The influence of reactive power for AMMR PTO

For a non-rectification PTO, reactive power is known to be indispensable to achieving the maximum power set by impedance matching. But it is unclear how much benefit reactive power has for a rectifier PTO. By introducing the position feedback gain K_I which supplies reactive power, it is found that reactive power does not have significant effects on the power of the AMMR PTO. Fig. 12 shows the optimal power with different K_I values. It can be seen that although using reactive power to stiffen the system can lead to larger power over short wave periods, this increase is less than 15 %. Moreover, the power drops slightly over long wave periods, likely counteracting the gains from the short period waves. Similar effects are observed with positive K_I that softens the system, in which case there is slight increase over long wave periods and slight decrease over short wave periods. Considering the fact that reactive power often entails larger required generator currents and torque, it is more desirable to only draw active power from the

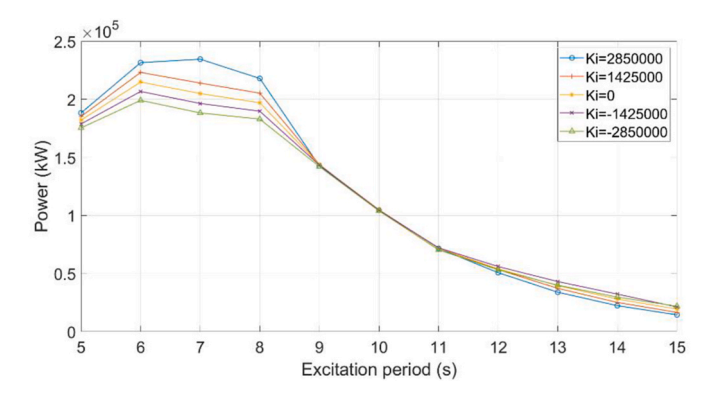


Fig. 12. Power comparison between different K_I levels.

generator. The power performance of $K_I=0$ shows that the AMMR PTO can achieve close to optimum power with only damping control of K_p , indicating its unique advantage of maximizing power without incurring reactive power flow. In the following sections, more analysis is performed with only the active damping power to quantify the effects of control parameters and wave conditions.

(3) Control parameters sensitivity with respect to wave periods

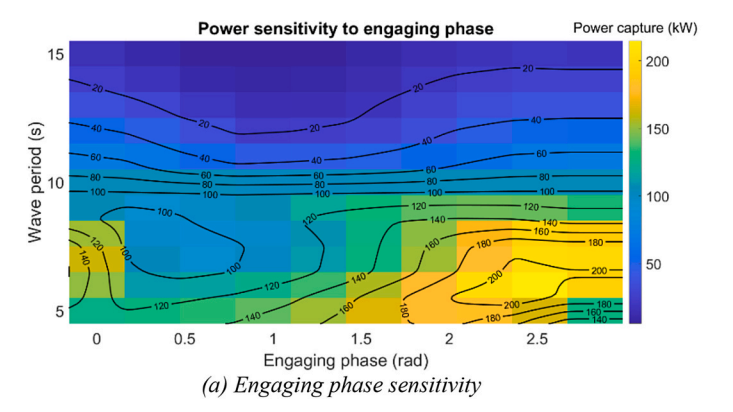
For an active power damping only control of the AMMR WEC, the control parameters are the engaging timing, engaging duration and generator damping torque. Since the power is nonconvex with respect to these parameters and the combination of parameter space is very large, it is important to determine the sensitivity of the power to changes in the parameters. An analysis on regular waves sheds some light on the effects of shifting control parameters. Fig. 13 (a) shows the sensitivity of engaging phase φ over different wave periods. It is seen that the power is at a similar level across different engaging phases at the resonance 10 s wave. As the wave periods get longer or shorter, the power begins to show larger differences across the whole engaging phase range. However, the power value is only sensitive around a narrow range of phase values, and remains at similar levels within relatively wide phase ranges. In summary, for each wave period there are a high-power phase range and a low-power phase range. The high-power range of short waves is generally narrower than that of longer waves, but still wide enough that 1 radian phase shift from the optimum decreases power by less than 20 %. Fig. 13 (b) shows the sensitivity of engaging duty cycle d over different wave periods. Again, for the 10 s wave, the power is at the same level regardless of duty cycle. The power shows larger difference across different duty cycle values as wave periods get longer or shorter. The sensitivity of power as the duty cycle shifts is generally mild, with power remaining at similar levels in certain ranges of duty cycle values. The optimum power range for short waves is narrower and covers smaller

duty cycles, while the optimum power range for long waves is wider and extends to medium duty cycles. Overall speaking, 30%–50 % duty cycle can achieve a high-power level for all the wave periods, and larger engaging duty cycle generally decreases power except near the resonance period.

Fig. 14 shows the generator damping coefficient's sensitivity at different wave periods. A clear trend can be seen from the resonance 10 s wave to shorter and longer wave periods. At the resonance period, power remains at the same level across the whole K_p value range. As the wave period shifts away, there still is a wide band of K_p value range that produces high power. The upper bound of that band is always at the high end of K_p values, while the lower bound gradually moves from small K_p values to medium K_p values as wave periods get shorter or longer. Clearly, a medium to high K_p value can guarantee a high power output across different wave periods. From the sensitivity analysis above, control strategies can be adapted accordingly when wave conditions change. When dominant wave periods become shorter, duty cycles should generally be tuned shorter and generator damping should be tuned larger. While when wave periods get longer, duty cycles need to increase as well as the generator damping. In realistic irregular waves, the engaging phase needs to be decided on a wave-to-wave basis with some sort of wave prediction. In short waves this timing is more sensitive than longer waves and needs finer discretization when it comes to discrete control optimization.

(4) Analysis of AMMR WEC trajectories

To understand why and how the switching effects of AMMR increase power generation and to see if there are any conflicts between the goal of power maximization and motion rectification, a detailed analysis of the AMMR WEC's trajectories is needed. Three sets of trajectories corresponding to wave periods 5s, 10s and 15s are analyzed to show how the AMMR PTO works at and outside the resonance frequency. Fig. 15 first shows the optimal trajectories of three duty cycle levels at the resonance 10s wave. Note from Fig. 13(b) that the generated power is similar for these three duty cycle levels. This can be explained by observing the excitation force and WEC velocity trajectories. Despite the engaging duration differences, in all three cases the resulting flap velocity is almost in phase with the excitation force. This greatly amplifies the absorption of input wave power as shown in Fig. 15(d), where the enclosed area of the excitation-displacement loop represents the input wave energy over one wave period. Also, a comparison with the nonswitching conventional PTO (100 % duty cycle) demonstrates the AMMR PTO's capability of amplifying the WEC's motion. This comes from the unique dynamics of switching phenomenon which can align the WEC structure's motion to be in phase with the wave force without the need of the generator drawing reactive power. What's even more attractive about this switching phenomenon is its flexibility of engaging duration. For this 10 s wave example, 80 % duty cycle engaging duration



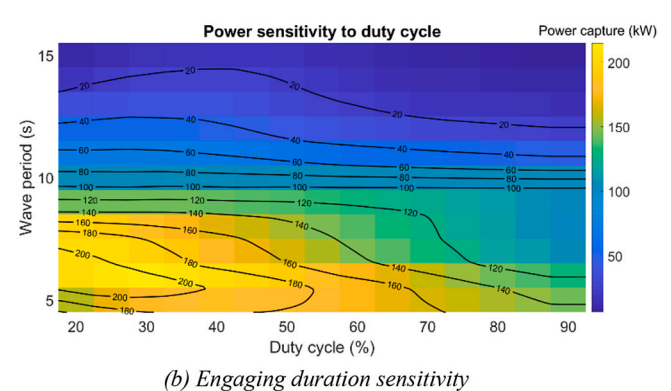


Fig. 13. Power sensitivity with respect to switching time control parameters.

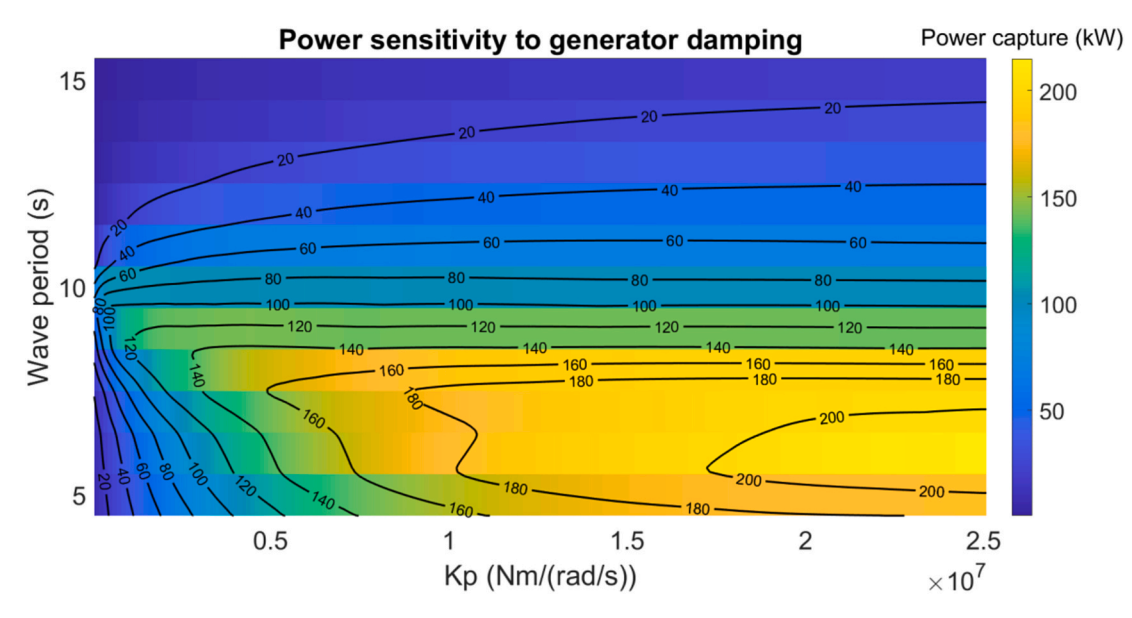


Fig. 14. Power sensitivity with respect to generator damping coefficient Kp.

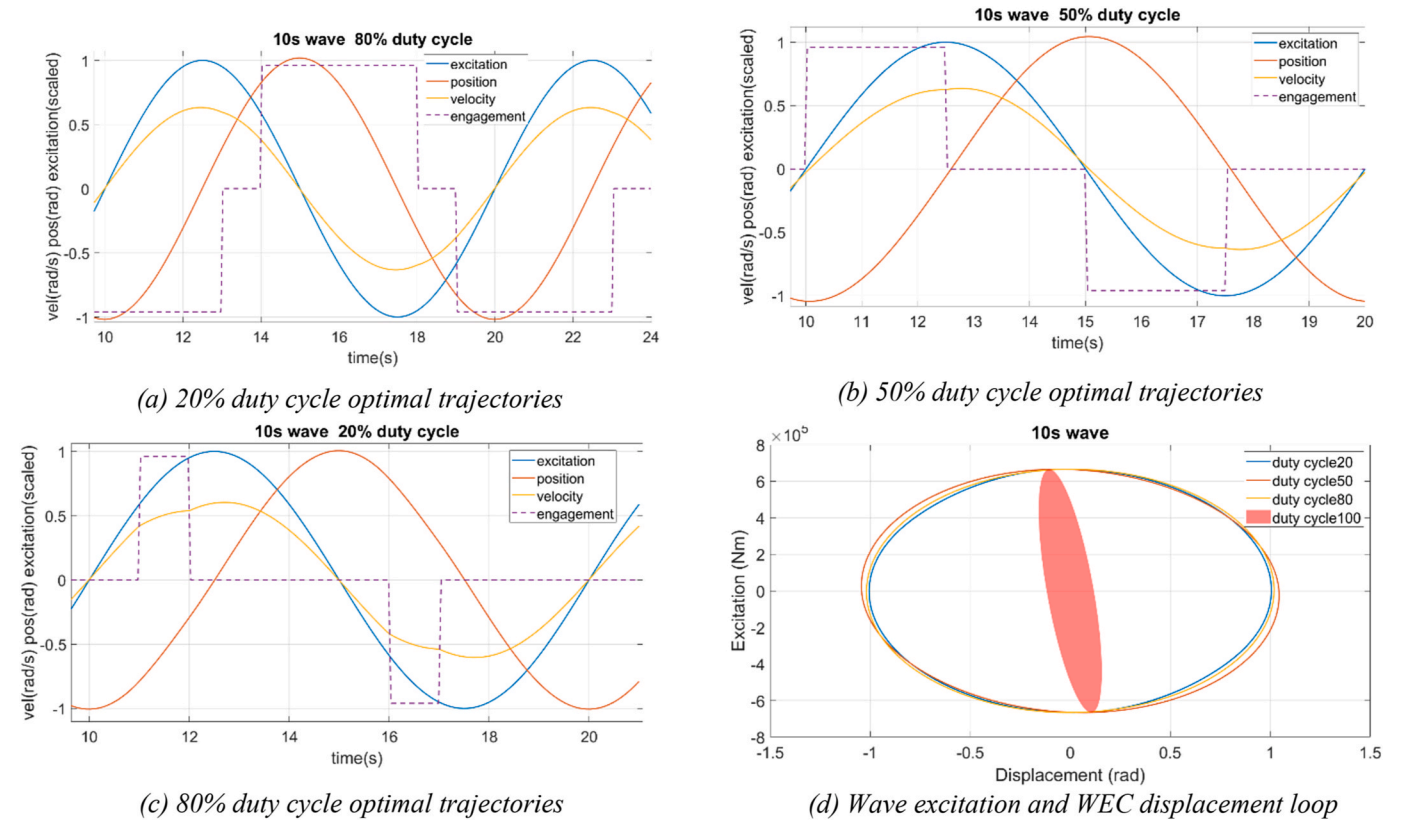


Fig. 15. AMMR WEC trajectories under 10 s wave.

gives the most power. However, the motion cannot be rectified since the flap reverses direction during the engaging stage. After decreasing the duty cycle to 20 %, rectification can be easily performed. Also, by increasing the generator damping coefficient and shifting the engaging phase, the power only decreases slightly. This makes it possible to maximize power and rectify motion at the same time.

Fig. 16 shows the optimal trajectories of 5 s wave. This is the wave period where AMMR PTO significantly boosts power compared to other PTOs. Among the three duty cycle levels, 50 % duty cycle gives more

power output. This can be attributed to a better aligned phase between wave excitation force and flap velocity, which implies an effective control of the switching times of the clutches should target a WEC velocity in phase with the excitation. For short waves such as in this example, the optimal control takes a declutching pattern [41], where the flap is disengaged from the PTO at a low speed to gain speed and then PTO is engaged at a high speed with large damping to take out power. With the optimal duty cycle around only 50 %, it is also easy to perform rectification for this short wave.

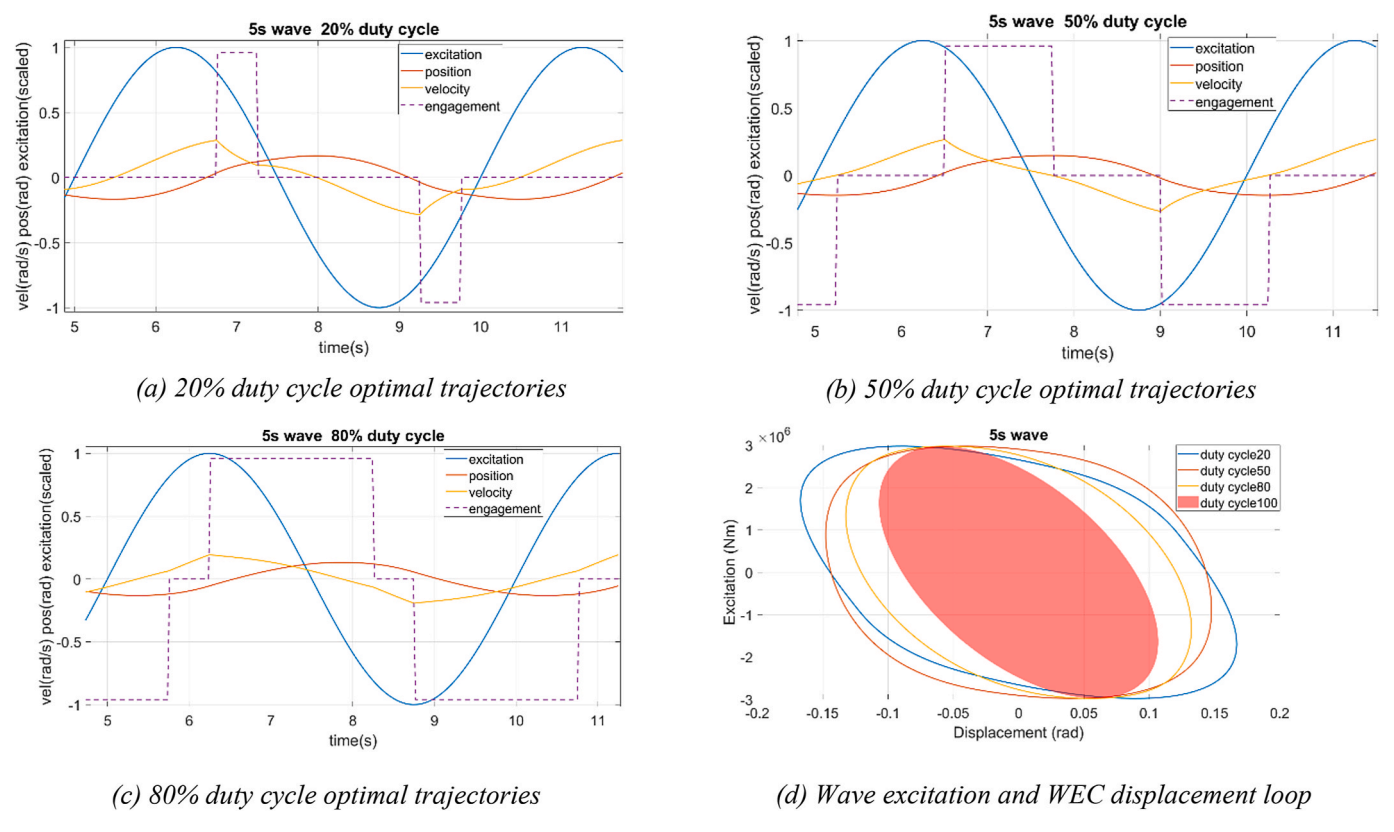


Fig. 16. AMMR WEC trajectories under 5 s wave.

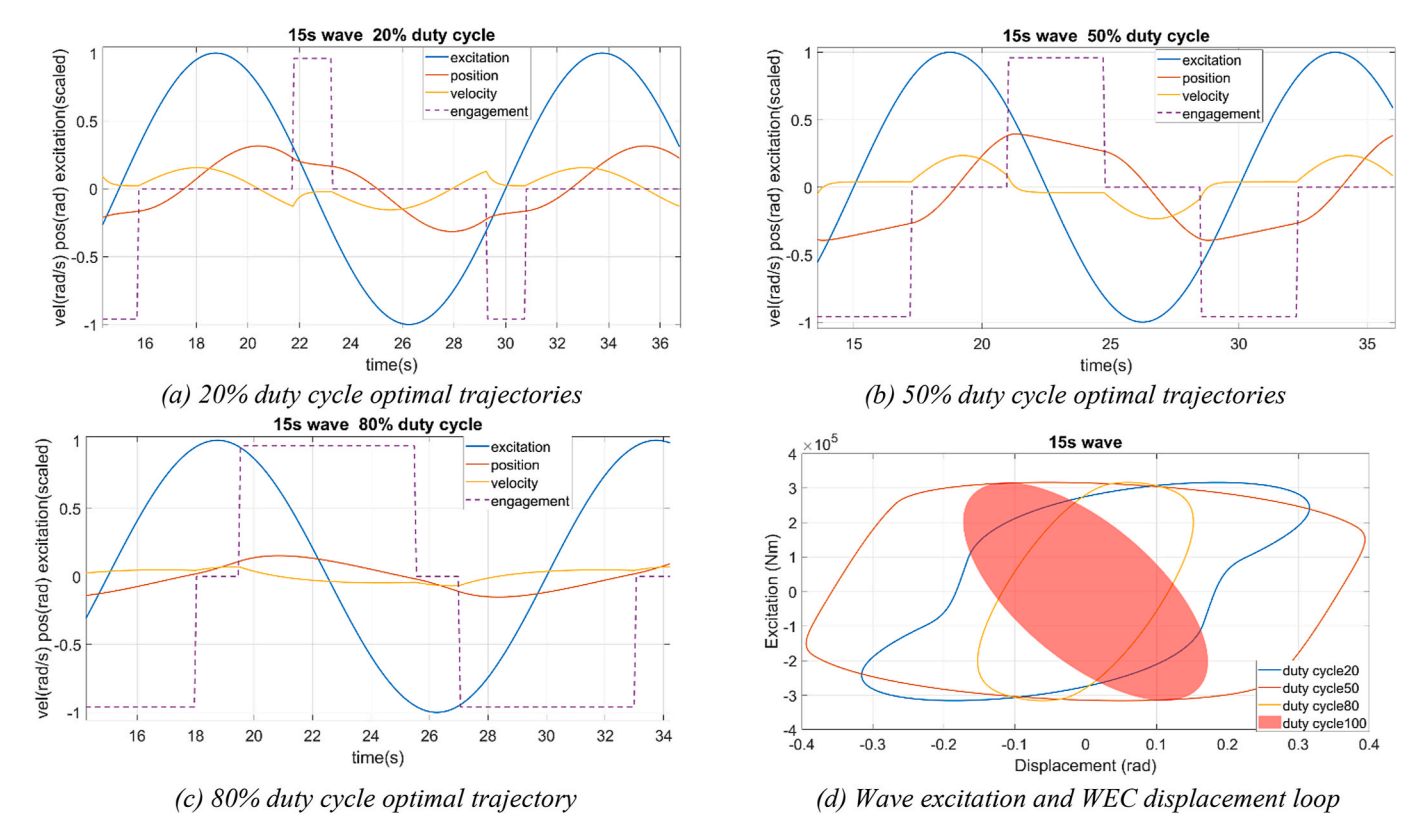


Fig. 17. AMMR WEC trajectories under 15 s wave.

Fig. 17 shows the optimal trajectories of 15 s wave. This is the wave period where the designed flap has the smallest power potential due to small wave excitation force. Still, with proper engaging control the AMMR PTO is able to triple the power compared to non-switching PTOs. But the power is more sensitive to the duty cycle at this wave period. 50 % duty cycle gives much more power than the other two duty cycle levels. By examining the corresponding trajectories, it appears the optimal switching pattern resembles a latching strategy [42]. During the engaging stage, a large generator damping is applied and the flap moves very slowly as if it is latched, then after disengaging it swiftly crosses to the other side and gets engaged again when its velocity drops close to zero. The difference from latching control is that with AMMR the power is generated during the latched stage instead of the unlatched stage, because during engaged stage the flap still has a slow velocity. The problem with this control pattern is that it is not compatible with the goal of rectification, since engaging must happen around low speed. Although it is possible to start engaging after the flap's velocity crosses zero, this may sacrifice some potential power gains.

5.3. Tank experiment validation

The proposed AMMR gearbox was fabricated and tested with a 1:10 scaled down prototype of the flap considered in the case study. The experiment setup in the wave tank is shown in Fig. 18. The flap hinge at the bottom was fixed to a frame that was anchored on two heavy I-beams on the tank floor. The PTO was set on a platform hanged above the water and its input shaft was driven by a belt transmission connected to the flap. A torque sensor is located right after the belt pulley to measure the torque from the flap. A high precision encoder is mounted on the other side of the pulley to measure the flap's velocity. Note that all the shaft measurements are scaled back to the flap torque and velocity by a pre-calibrated belt transmission ratio (1:66). The input motion is amplified again with a 1:3.5 gearbox before the AMMR PTO. The equipment used for the experiment is listed in the Appendix Table A1. The engagement of electromagnetic clutches in the AMMR gearbox were controlled through two solid state relays (SSR) while the generator's torque was controlled by a servo drive using space vector pulse width modulation (SVPWM). The control program was implemented using a dSPACE real-time machine, which outputs analog signals to control the SSRs and uses CAN signals to

 Table 2

 AMMR Optimal power and control parameters in experiments.

Wave period	AMMR power	Generator damping	Duty cycle	Phase
1.5 s	8 Watt	0.004 Nms/rad	70 %	2.3 rad
2 s	7.2 Watt	0.003 Nms/rad	70 %	2.5 rad
2.5 s	5.2 Watt	0.0015 Nms/rad	50 %	3 rad
3 s	4 Watt	0.0008 Nms/rad	50 %	1.6 rad
3.5 s	2.5 Watt	0.002 Nms/rad	50 %	1.8 rad
4 s	1.5 Watt	0.003 Nms/rad	50 %	0.3 rad
4.5 s	0.55 Watt	0.003 Nms/rad	50 %	0.5 rad
5 s	0.82 Watt	0.004 Nms/rad	50 %	2.6 rad

communicate with the drive. During the tests, the clutch switching times and control gains of the generator were tuned manually to find the optimal power. The wavemaker control signals were pre-calibrated before the tests by placing a wave probe at the location of the flap installation so that desired wave conditions (height and period) can be generated accurately for the test spot. The wave excitation torque acting on the flap was estimated by performing a latched flap test. Specifically, the flap was locked by engaging both clutches when running the waves. The torque sensor then recorded the excitation torque. In the meantime, a wave probe located roughly 10 feet upstream recorded the wave height. A relationship between wave heights and excitation torques in the frequency domain was then derived using Fourier transform and used to estimate the excitation torque from wave heights in the control tests.

According to Froude scaling law, the corresponding wave periods for 5–15 s at 1:10 scale device are 1.58–4.74 s. Therefore, eight wave periods from 1.5 s to 5 s are investigated and the corresponding optimal power and control parameters obtained in the experiments are summarized in Table 2. All the waves have the same 10 cm wave height as scaled down from the 1 m wave height in the full scale. It is observed that the optimal power trend is similar to that of the full-scale analysis, with the peak power obtained in the shortest wave instead, indicating an excitation dominant system. The optimal generator damping is the smallest around the resonant 3 s wave and becomes larger as waves get shorter or longer, showing the same trend as the full-scale analysis. The optimal duty cycle at short waves is much larger than the full-scale analysis. This is due to insufficient available generator damping in the experiments. For example, the generator damping can only be set at a maximum 0.004

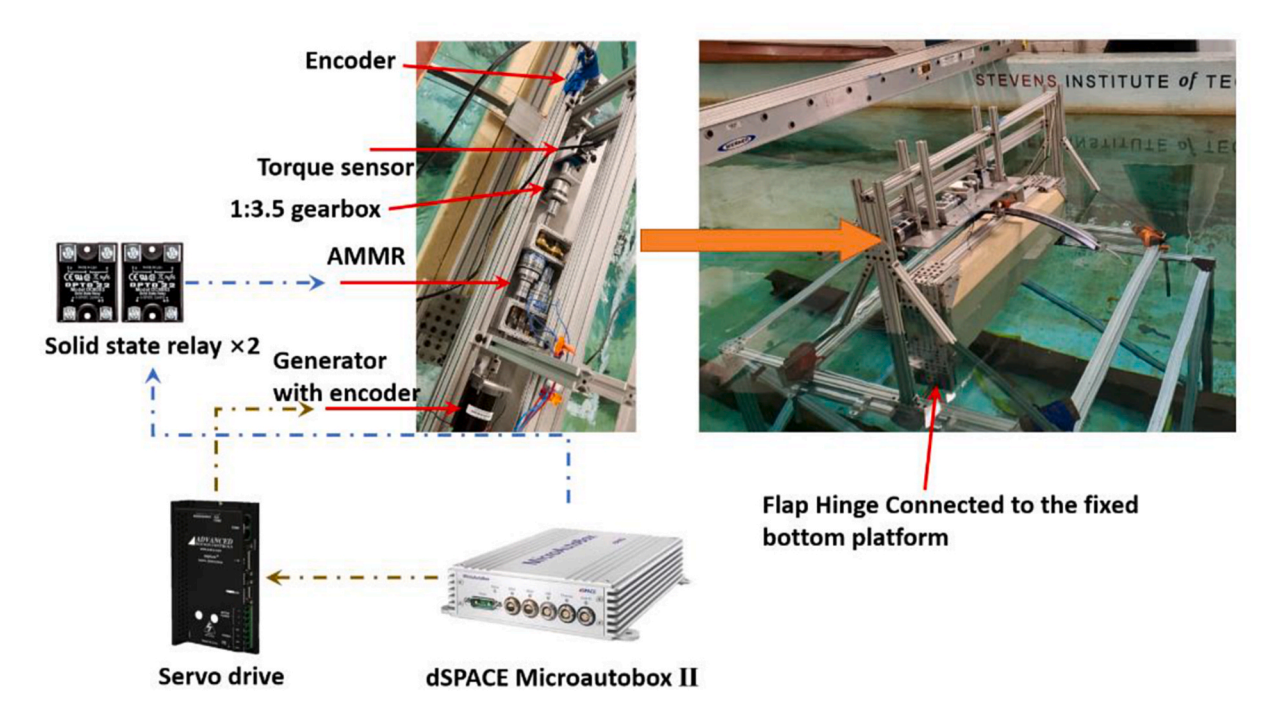


Fig. 18. Integrated tank validation experiment setup.

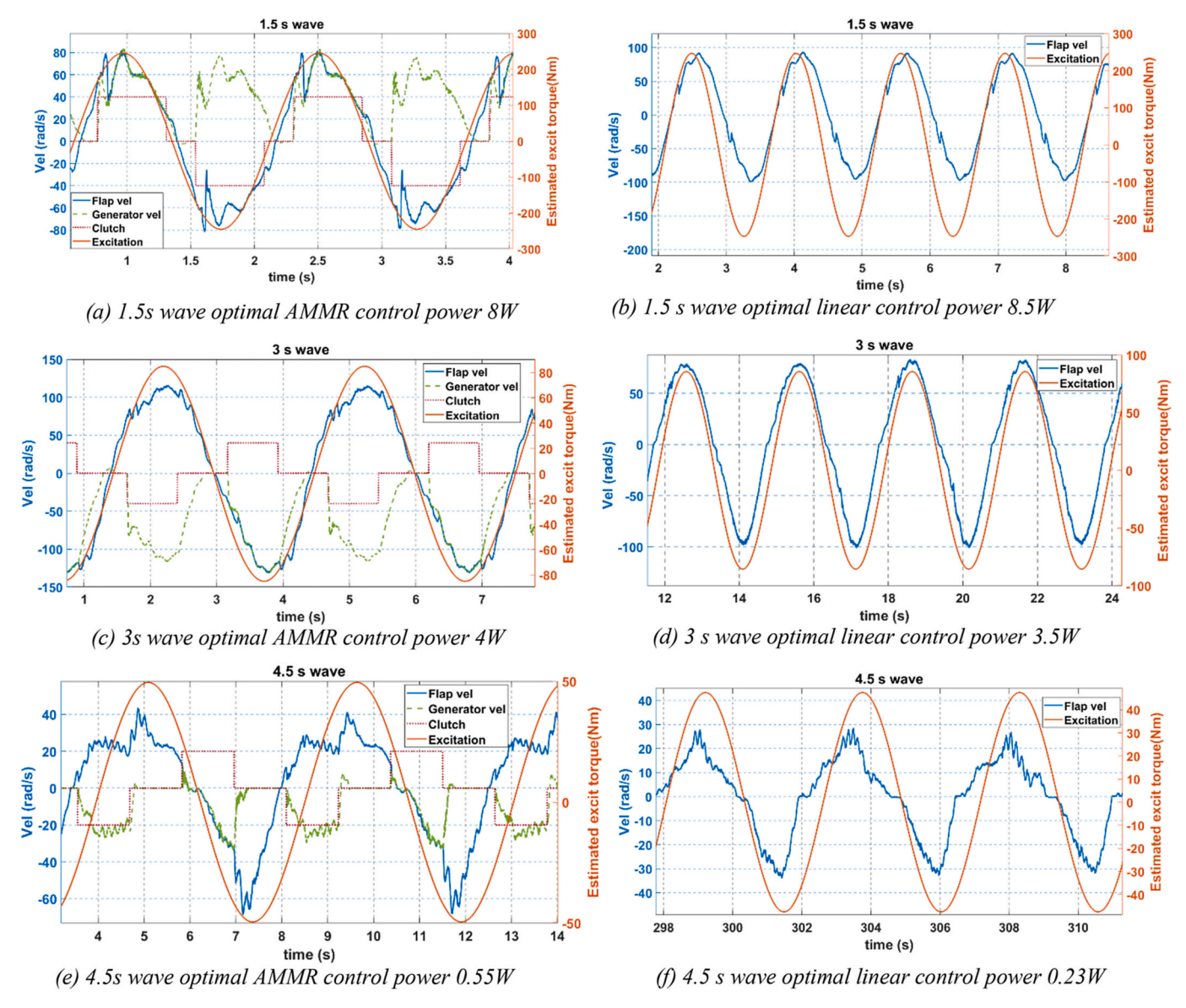


Fig. 19. Optimal trajectories obtained in the tank tests for AMMR and linear PTO.

Nms/rad for the 1.5 s wave. At this damping level, the peak generator velocity is about 280 rad/s, and 1.12 Nm damping torque needs to be applied. This is almost 3 times the generator's rated 0.44 Nm torque and can only last temporarily. Since maximum damping is limited, more engaging time is required to achieve the same power level. Other than this, the optimal duty cycle and phase values agree reasonably well with the full-scale analysis. The optimal trajectories observed in the experiments for three typical wave periods are presented in Fig. 19. The plots on the left side show the trajectories under optimal AMMR control while the plots on the right show the trajectories of a non-switching PTO where one clutch is always engaged. For the non-switching linear PTO, only the proportional control gain is tuned for the largest power.

Note that in Fig. 19, the flap's velocity is multiplied by the transmission gear ratio for ease of visualization, so it's essentially the bidirectional velocity at the AMMR gearbox input shaft. It is noted that in comparison with a linear PTO, the AMMR PTO significantly amplifies the motion of the flap, allowing the generator to rotate at a higher velocity. As for the mechanical power absorbed, the AMMR achieves comparable power performance as the linear PTO in short waves and can capture more power than the linear PTO when wave periods get longer. It is worth mentioning here that the optimal trajectory at 1.5 s short wave is a little

different from what is suggested in the numerical analysis of Subsection 5.2. The numerical analysis suggests a declutching pattern of control, where the generator engages at high speeds and applies large damping towards low speeds. However, in the experiments the optimal engagement happens at lower speeds and the engaging duration lasts longer. This is due to the limitation on the largest damping the generator can apply, which negatively impacts the optimal power that is obtained in the experiments. Although sacrificing some power absorption, this pattern of control is easier to implement in practice as engaging at lower speeds generally does not incur large clutch impacts or require the generator to rapidly accelerate. Other than this short wave period, optimal clutch control patterns similar to the numerical analysis were observed for other wave periods, especially over the long wave periods, where it is best to engage the generator and disengage it at low speeds to let the flap swing further. Overall, the experiments show good agreement with the numerical results and demonstrated the proposed design's effectiveness. Still, several constraints present in the current experimental implementation limit the attainable maximum power. Notably, the friction in the mechanical transmission is larger than expected. Larger viscous damping leads to an overdamped system, which reduces the flap's oscillation amplitude. Larger stiction and coulomb friction cause nonsmooth motion of the flap, further increasing the system's nonlinearity and reducing the predictability of the numerical model. Better fabrication and alignment of the mechanical PTO are needed to reduce the friction, but at a small scale it is hard to reduce the friction level to a point that is representative of the full scale. Another constraint comes from the limited encoder resolution. Ideally, the speeds on the two sides of AMMR should be synchronized before engaging. As encoders' resolutions are low, in reality the speeds difference cannot be controlled well. Therefore, the generator inertia has to be kept minimal to avoid large impacts due to engaging at different speeds. This limitation prevents us from investigating more on the generator inertia effects experimentally.

6. Discussions

Traditionally, generators' inertia plays an important role in smoothing out power. For wave energy converters with direct mechanical transmissions, the rigid connection between the generator and the floater means that the generator constantly reverses rotating direction with the floater's oscillations. Therefore, power fluctuation is large and mechanical and electrical components are over designed to be bulky and costly. With mechanical motion rectification, the generator's output power can be greatly smoothed. Ideally, the larger the inertia, the smoother the power is, and the less power conditioning would be required. However, generator inertia also influences the WEC's power capture, which indicates that the inertia value should be chosen based on a tradeoff between power fluctuation level and average recovered power. Interestingly, the case study presented in this paper implies that generator inertia's impact on power capture can be minimized through proper control, which is enabled by the proposed new active motion rectification mechanism (AMMR). This motivates the need for further studies on control co-design of the generator inertia, or even control co-design of the floater geometry since the influence of the floater's added mass needs to be reconsidered as well. The method presented in this paper serves as a convenient tool for conducting such co-design analysis for individual frequencies across a targeted spectrum. Still, for random irregular sea conditions, a more practical control algorithm would need to be designed to maximize average power capture while satisfying certain power variation constraints. Another aspect that needs further investigation is the effect of PTO efficiency. In this paper it is assumed the wave power captured is equal to the harvested power, which implies a loss free power takeoff. However, in reality PTO is not loss free and has different efficiencies depending on the WEC's operation conditions. For example, for the mechanical PTO considered in this paper, there are different mechanical transmission losses depending on the velocity profile. The generator also has different copper losses and iron losses depending on the applied torque and its rotational speed. Considering these losses will allow a more accurate and realistic estimate of the true useful power that can be harvested from a device. This paper also follows the convention in assuming accurate generator torque control and neglecting the detailed control implementation in power electronics [43]. Since the generator's mean velocity can be increased after motion rectification, additional benefits/opportunities may be found when taking the power electronics control into consideration. However, when considering more realistic PTO and power converters, the design optimization becomes much harder and likely needs to use some heuristic optimization methods [44].

7. Conclusions

An active mechanical motion rectifier (AMMR) design for mechanical PTO of wave energy converters (WEC) was proposed, designed, analyzed and experimentally validated. The new design is inspired by active electrical rectifiers and has more control freedom than a passive MMR. Along with the new design, a compatible computational approach was developed for evaluating the power capture of the nonlinear WEC using the new AMMR-based PTO. This method directly solves the steady-state controlled

response of the WEC, thus eliminating the need of expensive time-domain simulations and allowing for power optimization. A case study of a flaptype oscillating surge wave energy converter demonstrated the effectiveness of this approach. For the investigated flap WEC, optimally controlled AMMR-based PTO was found to outperform the previous MMR PTO in terms of power capture by 2-3 folds depending on the wave periods. Moreover, it was found that with active clutch control the generator's inertia does not have as large influences on the power capture as the passive MMR. It was also shown that using generator reactive power leads to less than 15% increase in power capture, suggesting passive damping force alone can achieve good power performance for the WEC with AMMR PTO. Optimal trajectories show a declutching and a latching control pattern for short and long wave periods respectively, sometimes contradicting the rectification requirement. In addition, sensitivity analysis indicates there exist control intervals where power remains within 20 % of the optimum when the control parameters vary. This provides some guidance for optimizing control parameters under an irregular wave situation. Finally, scaled down tank tests showed the new AMMR design is effective and works as predicted by the numerical analysis. There are three aspects that need further investigations in the future work to realize the full potential of this new design. First, the mechanical PTO is assumed ideal in this paper to focus on the clutch effects. More realistic modelling of the drivetrain as well as the electric generator is needed to incorporate various losses in assessing the PTO's power potential. Second, there is a need to develop a more efficient method to evaluate the power potential of a certain PTO design. Currently a costly parameter sweeping is still required to evaluate each design option. Based on the patterns of optimal trajectories identified in this paper, it may be possible to find a more efficient way to approximate the regular wave optimal control without enumerating different control parameter combinations. Finally, in order to use the AMMR-based PTO efficiently in realistic random seas, controllers suitable for real-time implementation under irregular waves needs to be designed. The generator's inertia needs to be co-designed with the corresponding controller to strike a balance between power maximization and power smoothing.

CRediT authorship contribution statement

Lisheng Yang: Writing – review & editing, Writing – original draft, Visualization, Validation, Software, Methodology, Investigation, Formal analysis, Data curation, Conceptualization. Jianuo Huang: Writing – review & editing, Visualization, Validation, Investigation, Data curation, Conceptualization. Jia Mi: Writing – review & editing, Software, Project administration, Investigation, Data curation. Muhammad Hajj: Writing – review & editing, Supervision, Resources, Project administration, Funding acquisition. Giorgio Bacelli: Writing – review & editing, Supervision, Formal analysis. Lei Zuo: Writing – review & editing, Supervision, Resources, Project administration, Investigation, Funding acquisition, Conceptualization.

Declaration of competing interest

The authors declare that they have no known competing financial interests or personal relationships that could have appeared to influence the work reported in this paper.

Acknowledgements

The authors wish to thank the financial support partially from the US NSF Grant # 2152694, USDOE WPTO Grant# Number DE-EE0008953, and USDOE SNL seedling project through Grant #DE-NA0003525. This paper describes objective technical results and analysis. Any subjective views or opinions that might be expressed in the paper do not necessarily represent the views of the US DOE, NSF, or the United States Government.

Appendix

Table A.1
Experiment equipment lists

Equipment name	Reference	
dSPACE controller	dSPACE Microautobox II	
Servo drive	Advanced Motion Control DPCANTE-060b080	
Generator	Anaheim Automation BLWS235D-36V-4000	
Gearbox (1:3.5)	GYSIN Gearbox GPL042	
Electromagnetic clutch	Ogura Clutch AMC-20	
Solid state relay	Opto22 DC60S3	
Torque sensor	ATO torque sensor ATO-TQS-DYN-205 3Nm version	
Flap side encoder	SICK DFS60B-TFPA10000	
Generator encoder	Anaheim Automation ENC-A2I-1250	

References

- M. Lehmann, F. Karimpour, C.A. Goudey, P.T. Jacobson, M.-R. Alam, Ocean wave energy in the United States: current status and future perspectives, Renew. Sustain. Energy Rev. 74 (2017) 1300–1313.
- [2] R.G. Coe, G. Lavidas, G. Bacelli, P.H. Kobos, V.S. Neary, Minimizing cost in a 100% renewable electricity Grid: a case study of wave energy in California, in: International Conference on Offshore Mechanics and Arctic Engineering, vol. 85932, American Society of Mechanical Engineers, 2022 V008T09A079.
- [3] S. Parmeggiani, J.F. Chozas, A. Pecher, E. Friis-Madsen, H. Sørensen, J.P. Kofoed, Performance assessment of the wave dragon wave energy converter based on the EquiMar methodology, in: 9th Ewtec 2011: Proceedings of the 9th European Wave and Tidal Conference, Southampton, UK, 5th-9th September 2011, University of Southampton. 2011.
- [4] A.F. Falcão, J.C. Henriques, Oscillating-water-column wave energy converters and air turbines: a review, Renew. Energy 85 (2016) 1391–1424.
- [5] P. Benreguig, M. Vicente, A. Dunne, J. Murphy, Modelling approaches of a closed-circuit OWC wave energy converter, J. Mar. Sci. Eng. 7 (2) (2019) 23.
- [6] B. Joensen, H.B. Bingham, R. Read, K. Nielsen, J.B. Trevino, Performance predictions of one-way energy capture by an oscillating water column device in Faroese waters, in: 14th European Wave and Tidal Energy Conference (EWTEC 2021), 2021, p. 2117.
- [7] J. Henriques, J. Portillo, W. Sheng, L. Gato, A.d.O. Falcão, Dynamics and control of air turbines in oscillating-water-column wave energy converters: analyses and case study, Renew. Sustain. Energy Rev. 112 (2019) 571–589.
- [8] M. Saad, M.G. Díaz, B. Pereiras, J. González, Optimized geometry design of a radial impulse turbine for OWC wave energy converters, Appl. Ocean Res. 111 (2021) 102650.
- [9] T.K. Das, E. Kerikous, N. Venkatesan, G. Janiga, D. Thévenin, A. Samad, Performance improvement of a Wells turbine through an automated optimization technique, Energy Convers. Manag. X 16 (2022) 100285.
- [10] A.T. Koth, M.A. Nawar, Y.A. Attai, M.H. Mohamed, Performance enhancement of a Wells turbine using CFD-optimization algorithms coupling, Energy 282 (2023) 120062.
- [11] M.A. Jusoh, M.Z. Ibrahim, M.Z. Daud, A. Albani, Z. Mohd Yusop, Hydraulic power take-off concepts for wave energy conversion system: a review, Energies 12 (23) (2019) 4510.
- [12] A.F.d.O. Falcão, Modelling and control of oscillating-body wave energy converters with hydraulic power take-off and gas accumulator, Ocean engineering 34 (14–15) (2007) 2021–2032.
- [13] C. Cargo, A. Hillis, A. Plummer, Optimisation and control of a hydraulic power take-off unit for a wave energy converter in irregular waves, Proc. Inst. Mech. Eng. A J. Power Energy 228 (4) (2014) 462–479.
- [14] P. Ricci, et al., Control strategies for a simple point-absorber connected to a hydraulic power take-off, in: Proceedings of 8th European Wave and Tidal Energy Conference, Uppsala, Sweden, 2009, pp. 7–10.
- [15] R.H. Hansen, M.M. Kramer, E. Vidal, Discrete displacement hydraulic power takeoff system for the wavestar wave energy converter, Energies 6 (8) (2013) 4001–4044.
- [16] C. Liu, et al., A novel discrete control for wave energy converters with a hydraulic power take-off system, Ocean Engineering 249 (2022) 110887.
- [17] J.A. Leon-Quiroga, G. Bacelli, D.D. Forbush, S.J. Spencer, R.G. Coe, An efficient and effective WEC power take-off system, IEEE Trans. Sustain. Energy 14 (3) (2023) 1526–1539.
- [18] K. Rhinefrank, et al., Comparison of direct-drive power takeoff systems for ocean wave energy applications, IEEE J. Ocean. Eng. 37 (1) (2011) 35–44.
- [19] G. Bacelli, S.J. Spencer, D.C. Patterson, R.G. Coe, Wave tank and bench-top control testing of a wave energy converter, Appl. Ocean Res. 86 (2019) 351–366.

- [20] D.T. Gaebele, C.A. Michelén Ströfer, M.C. Devin, J.T. Grasberger, R.G. Coe, G. Bacelli, Incorporating empirical nonlinear efficiency into control Cooptimization of a real world heaving point absorber using WecOptTool, in: International Conference on Offshore Mechanics and Arctic Engineering, vol. 86908, American Society of Mechanical Engineers, 2023 V008T09A067.
- [21] H.-X. Zou, et al., Mechanical modulations for enhancing energy harvesting: principles, methods and applications, Appl. Energy 255 (2019) 113871.
- [22] C. Liang, J. Ai, L. Zuo, Design, fabrication, simulation and testing of an ocean wave energy converter with mechanical motion rectifier, Ocean Engineering 136 (2017) 190–200.
- [23] X. Li, et al., A compact mechanical power take-off for wave energy converters: design, analysis, and test verification, Appl. Energy 278 (2020) 115459.
- [24] B. Jiang, et al., Performance analysis and tank test validation of a hybrid ocean wave-current energy converter with a single power takeoff, Energy Convers. Manag. 224 (2020) 113268.
- [25] Y. Yang, P. Chen, Q. Liu, A wave energy harvester based on coaxial mechanical motion rectifier and variable inertia flywheel, Appl. Energy 302 (2021) 117528.
- [26] J. Wu, L. Qin, N. Chen, C. Qian, S. Zheng, Investigation on a spring-integrated mechanical power take-off system for wave energy conversion purpose, Energy 245 (2022) 123318.
- [27] F. Zhu, P.J. Antsaklis, Optimal control of hybrid switched systems: a brief survey, Discrete Event Dyn. Syst. 25 (2015) 345–364.
- [28] J.V. Ringwood, G. Bacelli, F. Fusco, Energy-maximizing control of wave-energy converters: the development of control system technology to optimize their operation, IEEE control systems magazine 34 (5) (2014) 30–55.
- [29] J. Falnes, A. Kurniawan, Ocean Waves and Oscillating Systems: Linear Interactions Including Wave-Energy Extraction, Cambridge university press, 2020.
- [30] X. Xu, P.J. Antsaklis, Optimal control of switched systems based on parameterization of the switching instants, IEEE Trans. Automat. Control 49 (1) (2004) 2–16.
- [31] S.C. Bengea, R.A. DeCarlo, Optimal control of switching systems, Automatica 41 (1) (2005) 11–27.
- [32] M.S. Shaikh, P.E. Caines, On the hybrid optimal control problem: theory and algorithms, IEEE Trans. Automat. Control 52 (9) (2007) 1587–1603.
- [33] R.G. Coe, G. Bacelli, S. Olson, V.S. Neary, M.B. Topper, Initial conceptual demonstration of control co-design for WEC optimization, Journal of Ocean Engineering and Marine Energy 6 (4) (2020) 441–449.
- [34] J. Mi, Q. Li, M. Liu, X. Li, L. Zuo, Design, modelling, and testing of a vibration energy harvester using a novel half-wave mechanical rectification, Appl. Energy 279 (2020) 115726.
- [35] A. Chowdhary, A. Kumar, S.K. Singh, Design and analysis of an electro-magnetic clutch, International Journal of Progressive Research in Science and Engineering 1 (3) (2020) 89–95.
- [36] A.K. Singh, S. Kumar, B.N. Agrawal, P.K.S. Nain, Design and analysis of spur gear, helical gear, and bevel gear by using ANSYS, in: Advances in Manufacturing Technology and Management: Proceedings of 6th International Conference on Advanced Production and Industrial Engineering (ICAPIE)—2021, Springer, 2022, pp. 641–650.
- [37] J.A. Armesto, R. Guanche, F.d. Jesus, A. Iturrioz, I.J. Losada, Comparative analysis of the methods to compute the radiation term in Cummins' equation, Journal of Ocean Engineering and Marine Energy 1 (4) (2015) 377–393.
- [38] R.G. Coe, G. Bacelli, D. Forbush, A practical approach to wave energy modeling and control, Renew. Sustain. Energy Rev. 142 (2021) 110791.
- [39] A. Ahmed, et al., Performance characterization and modeling of an oscillating surge wave energy converter, Nonlinear Dynam. 112 (6) (2024) 4007–4025.
- [40] T. Whittaker, M. Folley, Nearshore oscillating wave surge converters and the development of Oyster, Phil. Trans. Math. Phys. Eng. Sci. 370 (1959) (2012) 345–364.
- [41] A. Babarit, M. Guglielmi, A.H. Clément, Declutching control of a wave energy converter, Ocean engineering 36 (12–13) (2009) 1015–1024.

- [42] A. Babarit, A.H. Clément, Optimal latching control of a wave energy device in regular and irregular waves, Appl. Ocean Res. 28 (2) (2006) 77–91.
 [43] A. Alnujaie, A. Berkani, K. Negadi, L. Hadji, M.H. Ghazwani, Enhancing the performance and coordination of multi-point absorbers for efficient power
- generation and grid synchronization control, Journal of Applied and
- Computational Mechanics (2024).
 [44] A. Shadmani, M.R. Nikoo, A.H. Gandomi, Robust optimization of PTO settings for point absorber wave energy converter, in: Handbook of Formal Optimization, Springer, 2023, pp. 1–19.